Discrete dipole model of radiative transfer in dense granular layers

Sanaz Vahidinia[1,2], Jeffrey N. Cuzzi[2], Bruce Draine[3], Essam Marouf[4]

[1]Corresponding author; NASA Postdoctoral Associate; [2]Space Science Division, Ames Research Center, NASA; [3]Astronomy Department, Princeton University; [4]Electrical Engineering Department, San Jose State University

We have developed a numerical Regolith Radiative Transfer (RRT) model based on the Discrete-Dipole Approximation (DDA), which iteratively solves the exact wave equations for a granular target in response to an incident plane wave and mutual interactions between all component grains. We extend the traditional DDA approach in two ways: the DDA target is laterally replicated using periodic boundary conditions, to represent a small piece of a nominally flat granular particle surface, and the emergent intensity is sampled in the near field of the target to avoid diffraction-like artifacts arising from its finite size. The approach is applicable in regimes for which the assumptions of current RRT models are invalid, such as wavelength-size particles which are closely packed. In this first paper we describe the technique and present tests and illustrative results for simple cases, using layers of varying filling fraction between 0.01 and 0.7, containing nominally spherical monomers of uniform composition (SiO_2). We motivate the results with a simple "toy model" of scattering by a target with multiple interfaces. The model is easily extended to layers of particles which are heterogeneous in composition and arbitrarily shaped.

1. Introduction

Interpreting remote observations of granular bodies is an important tool in determining the surface composition of all airless solid bodies in the solar system. The granular surfaces of these bodies are constantly fragmented and mixed by meteoroid impacts, and are referred to as regoliths. Regolith particles are often comparable to or smaller than the wavelength of interest, and are packed to varying degrees of porosity such that many particles are touching. Models by Conel (1969), Hapke (*eg.,* 1981, 1983, 1999), Lumme and Bowell (1981), Shkuratov et al (1999a,b), and others have had many successes, but make certain simplifying assumptions which are not valid in all regimes of interest, and consequently fail to match the appearance of the spectra of granular materials at certain wavelengths (Moersch and Christensen 1995; see also section 2 below). All widely used models are suspect when the grains

are *not* well-separated but indeed closely packed, violating the assumptions of independent particle scattering (see however Mishchenko 1994, Mishchenko and Macke 1997, Pitman et al 2005), and Hapke/Shkuratov models in particular become problematic when the regolith grains are *not* large compared to a wavelength. As the expectations of compositional determination by remote sensing, and in particular by thermal infrared spectroscopy, become more demanding, improved theories will be needed which are able to, at least, adequately represent the spectral properties of known samples. This calls for a theory that reproduces the spectra of known samples over a wide range of refractive indices, size/wavelength ratio, and porosity.

Modeling a regolith layer generally starts with calculating the single scattering properties (albedo and phase function) of an individual regolith grain, and then using one of several methods to derive the overall reflection and transmission of a semi-infinite layer composed of many similar grains. The approaches to date have been adapted from classical approaches to atmospheric radiative transfer. In clouds, for instance, individual scatterers are generally separated by many times their own size and the scattering behavior of an isolated particle is appropriate for modeling ensembles of these particles. The single scattering albedo can be calculated analytically for small particles in the Rayleigh limit, and Mie scattering is used for larger spherical particles. Semi-empirical adjustments can be made at this stage to allow for particle nonsphericity (Pollack and Cuzzi 1979), or more elaborate T-matrix calculations can be used (Waterman, 1965, Mishckenko et al. 1996). Mie scattering is cumbersome in the geometrical optics limit, but various ray-optics based approaches can be used here (Shkuratov 1999a,b, Mishchenko and Macke 1997, Hapke 1999).

Once the grain single scattering albedo ϖ_o and scattering phase function $P(\Theta)$ (the distribution of intensity with scattering angle Θ from the incident beam) are obtained, various multiple scattering techniques can be used to derive the properties of an ensemble of such particles in a layer. These techniques include the N-stream or discrete ordinates approach (Conel 1969), adding/doubling of thin layers (Hansen and Travis 1974, Wiscombe 1975(a,b), Plass 1973), or Chandrasekhar's X,Y, or H functions, for which tabulations and closed-form approximations exist in the case of isotropic scattering (Hapke 1981). A variety of "similarity transformations" can be used to convert arbitrary grain anisotropic scattering properties into their isotropic scattering equivalents (van de Hulst 1980; see Irvine 1975), allowing the use of these standard isotropic solutions.

Generally, these approaches assume the regolith grains have scattering properties which can be calculated in isolation. The independent scattering assumption is normally assumed to be satisfied when the particle spacing l is larger than several grain radii r_g (van de Hulst 1981)[1]; Hapke (2008) has extended this spacing constraint to be a function of the

[1]The source is a brief comment in section 1.21 of van de Hulst's book.

radius/wavelength ratio itself by adopting van de Hulst's assertion about the required spacing, and interpreting this spacing as a distance between surfaces of adjacent particles. This approach predicts that interference effects are not important in most regoliths when $r_g \gg \lambda$, but filling factors less than 0.1 are needed to validate incoherent, independent scattering when $r_g \sim \lambda$ (see Appendix A).

A number of theoretical and experimental studies have been conducted regarding the role of close packing effects for over fifty years. An early study found changes in reflectance with porosity depended on grain albedo (Blevin and Brown 1961). Some studies have concentrated on the dependence of *extinction* on porosity, without discussing the scattering or reflectivity of the medium (Ishimaru and Kuga 1982, Edgar et al 2006, Göbel et al 1995); these latter studies are valuable in indicating the porosity regime where packing effects become important (around 10% volume filling factor), but even this threshold is a function of particle size and wavelength (Ishimaru and Kuga 1982). As a partial attack on the close-packing problem, various approaches have been tried to treating the diffracted component of both the phase function and albedo as unscattered in the dense regolith environment (Wald 1994, Pitman et al 2005; see however Mishchenko 1994 and Mishchenko and Macke 1997 for cautionary notes). Other research has focussed on the Lorentz-Lorentz (EMT or Garnett) technique for fine powders and variants on hard-sphere packing positional correlation functions such as the Percus-Yevick static structure theory (Mishchenko 1994, Pitman et al 2005). These approaches are promising in some ways, but in other ways they degrade agreement with the data (Pitman et al 2005).

Few of these studies to date have attempted a combined treatment of variable refractive indices *and* porosity, but it is precisely this combination that leads to some of the most glaring failures of traditional models (see below). The formulation by Hapke (2008) suggests that increased filling factor almost always leads to increased reflectivity, unless the scattering grains have extremely high albedo $\varpi_o > 0.95$. Indeed, Blevin and Brown (1961) find that packing increases the reflectance of dark materials and decreases that of bright materials; however, the grain albedo threshold where the behavior changes may not be as high as modeled by Hapke (2008). Finally, many previous studies apply to regimes where the particle size is large compared to the wavelength.

Our approach can capture the combined role of size/wavelength (even when they are comparable), porosity, *and* refractive index. It avoids all of the common but frequently inappropriate simplifying assumptions by use of the discrete dipole approximation (DDA) to model radiative transfer in granular regoliths. In the DDA, scattering calculations are not limited by packing density, shape, or size of particles in the regolith. The technique has become more productive since its introduction (Purcell and Pennypacker 1973) due to a combination of increasing compute power and improved algorithms (*Draine and Flatau 2004, 2008*); com-

putational power remains its limiting factor, however. In section 2 we compare predictions of some current models with spectral data, to illustrate shortcomings of the models. In section 3 we describe our model, which has several novel aspects. In sections 4 and 5 we present some tests. In section 6 we give some preliminary results, and in section 7 give possible explanations and speculations.

2. Current model inadequacy: Thermal emission spectroscopy of SiO_2

Thermal emission spectroscopy is central to a new generation of planetary and astronomical exploration; moreover, it lies entirely in the problematic regime where the regolith grain size and separation are both comparable to the wavelength. Like nearly all treatments in the past, our models of emission spectroscopy start with reflectivities R, and relate them to emissivities E by the principle of detailed balance or Kirkhoff's law (Goody 1964; Linsky 1972); in the simplest case when both quantities are integrated over all incident and emergent angles, $E = 1 - R$. Analogous expressions can be derived when angle-dependent quantities are needed (see below).

Regolith scattering by grainy surfaces can be categorized by two or three major optical regimes defined by the refractive indices of the regolith material (see Mustard and Hays 1997 for a review). The first spectral regime is called "surface scattering" (at wavelengths where real and/or imaginary refractive indices, and surface reflectance, are large and the wave hardly penetrates into the material); *restrahlen bands* fall in this regime. The second regime is "volume scattering" (at wavelengths where the imaginary index is low and the real index is of order unity) which has a more moderate surface reflectivity; *transparency regions* result from this range of properties (Mustard and Hays 1997, MH97). Increasing the imaginary index in this refractive index regime increases absorption and decreases reflectivity. A third characteristic spectral property is a *Christiansen feature*, where the real index is equal to 1, so surface reflections vanish and the emissivity closely approaches unity. Mineral identification and grain size estimation from remote sensing data follow from modeling the shapes and relative strengths of these strong and weak spectral features.

As an exercise complementary to that of Moersch and Christensen (1995) we compared the performance of several typical RRT models against new laboratory measurements of thermal emissivity from layers of quartz grains with various sizes (data courtesy P. Christensen and J. Michalski). The data were taken at room temperature, and represent directional emissivities viewed roughly 30 degrees from the normal, with a field of view 30 degrees wide. Regolith samples were approximately 1 cm thick and their porosity is estimated by weighing as approximately 30% (P. Christensen, personal communication 2011). Our models used recent values of SiO_2 refractive indices from Wenrich and Christensen (1996) who (as did MC95) noted a discrepancy with the standard values of Spitzer and Kleinman (the

discrepancy apparently arises from tabulated values of oscillator parameters in Spitzer and Kleinman). In any case, we find that the differences in refractive indices - perhaps at the 10% level at the lowest values of imaginary index in transparency bands - have only a barely noticeable effect on the model results shown in figure 1. Since the SiO_2 refractive indices have now been measured twice independently, with the differences having a negligible effect on model results, this suggests that the model-data discrepancies in the transparency bands are *not* due to uncertainties in SiO_2 refractive indices but arise from a more profound cause.

Our three models are similar to those used by MC95 (one is identical) and will be seen to capture the same general behavior. All of our models used Mie theory to get the individual grain albedo ϖ_o, phase function $P_o(\Theta)$, and asymmetry parameter g_o directly from the refractive indices. This is because the first step of Hapke theory (using geometrical optics to get the grain albedo) is not justifiable here, where the grain size and wavelength are comparable. The asymmetry parameter $g_o = \langle \cos\Theta \rangle$ is a mean of $(\cos\Theta)$ over scattering angle Θ, as weighted by the phase function (see the review by Irvine 1975). To allow for the optical anisotropy of SiO_2, we computed grain properties separately using the ordinary (*ord*) and extraordinary (*ext*) ray refractive indices, and then obtained weighted grain averages using $\varpi_o = (2\varpi_{o,ord} + \varpi_{o,ext})/3$, and similarly for g_o.

Mie theory implicitly includes diffraction in ϖ_o, $P_o(\Theta)$, and g_o, because the particles are treated as isolated, independent scatterers, and for nearly all combinations of grain radius and wavelength, regolith grains are substantially forward scattering (see Hansen and Travis 1974, or Mishchenko and Macke 1997). Two of our models accept this behavior at face value. Both then obtain thick-layer solutions using very similar scaling relations. In one of the earliest attacks on this problem, Conel (1969) showed that a simple two-stream solution to the radiative transfer equation, taken to the limit of a semi-infinite layer, has a closed-form solution for hemispherical (flux) reflectivity R and emissivity $E = 1 - R$:

$$E = 1 - R = \frac{2}{u - 1}, \qquad \text{where} \tag{1}$$

$$u = \left(\frac{1 - \varpi_o g_o}{1 - \varpi_o} \right)^{1/2}. \tag{2}$$

MC95 present plots of results using this theory, although note a typo in the equation just below their equation 9 (compare Conel 1969, equations 10 and 15); our results for this and other models are shown in figure 1.

In our second model we use an empirical scaling transformation from van de Hulst (1980), which also starts with ϖ_o and g_o and derives a more detailed scaling relation for the integrated spherical albedo A of a large, smooth, regolith-covered particle, which is close to the hemispherical reflectivity R of a slab of its surface (see Cuzzi 1985):

$$E = 1 - R = 1 - \frac{(1 - s)(1 - 0.139s)}{1 + 1.17s}, \qquad \text{where} \tag{3}$$

$$s = \left(\frac{1-\varpi_o}{1-\varpi_o g_o}\right)^{1/2} = \frac{1}{u}. \quad (4)$$

The van de Hulst expression for E (equation 3) is basically a numerical refinement of Conel's two-stream expression (based on many comparisons with exact calculations), expanded to higher order in s, in that the van de Hulst $R \sim (1-s)/(1+s) = (u-1)/(u+1)$, which is exactly the Conel R, so it is not *entirely* independent but does enjoy some independent and exhaustive numerical validation.

In Hapke theory the diffraction lobe of the grain is explicitly neglected, to motivate isotropic scattering, which is then assumed for all orders of scattering except the first (for isotropic scattering the H-functions of Chandrasekhar are readily available). The validity of retaining or removing the diffraction contribution to the grain albedo and phase function has been debated in the literature (see Wald 1994, Wald and Salisbury 1995, Mishchenko and Macke 1997, and Pitman et al 2005). In fact, even if the diffraction lobe *per se* is arbitrarily removed, this does not necessarily imply the remainder of the scattering by the grain is isotropic (Pollack and Cuzzi 1979, Mishchenko and Macke 1997). However, for illustrating the state of widely used models, we include in figure 1 an H-function based emissivity as a placeholder for the full Hapke theory. Since we use Mie scattering to obtain ϖ_o and g_o, we transform these values to equivalent isotropic scattering albedos ϖ_i using a standard similarity transformation (Irvine 1975, and Hapke 1983 equation 10.25a):

$$\varpi_i = \frac{\varpi_o(1-g_o)}{1-\varpi_o g_o}. \quad (5)$$

For forward scattering particles, this transformation reduces the albedo and can be thought of as "truncating" or removing the diffraction peak. We then proceed to integrate the bidirectional reflectivity $R(\mu_o, \mu)$, which is a function of incidence angle θ_o and emission angle θ, where $\mu_o = \cos\theta_o$ and $\mu = \cos\theta$ (Chandrasekhar 1960):

$$R(\mu_o, \mu) = \frac{\varpi_i}{4\pi}\frac{\mu_o}{\mu_o+\mu}H(\mu_o)H(\mu) \quad (6)$$

over all incidence angles θ_o to derive the normal (hemispherical-directional) reflectivity $R(\mu = 1)$, using closed form expressions for H in Hapke 1983 (equations 8.22b, 8.25, and 8.57), and then set the corresponding emissivity $E(\mu = 1) = 1 - R(\mu = 1)$ (Goody 1964, Linsky 1972).

While the Mie-Conel and Mie-van de Hulst models are in the spirit of hemispherical emissivities (averaged over viewing angle), the Mie-H-function model is a directional emissivity (at normal viewing). As the experimental data used a beam of significant angular width, it is not clear whether either of these is to be preferred *a priori*. The Mie-Conel and Mie-van de Hulst approaches *accept* the forward-scattering nature of the grains as calculated by Mie theory, and the $H-$function (and Hapke) models effectively preclude it. Pitman et al (2005)

used a discrete ordinates code, rather than assuming isotropic scattering, and also found similar behavior before applying their packing corrections.

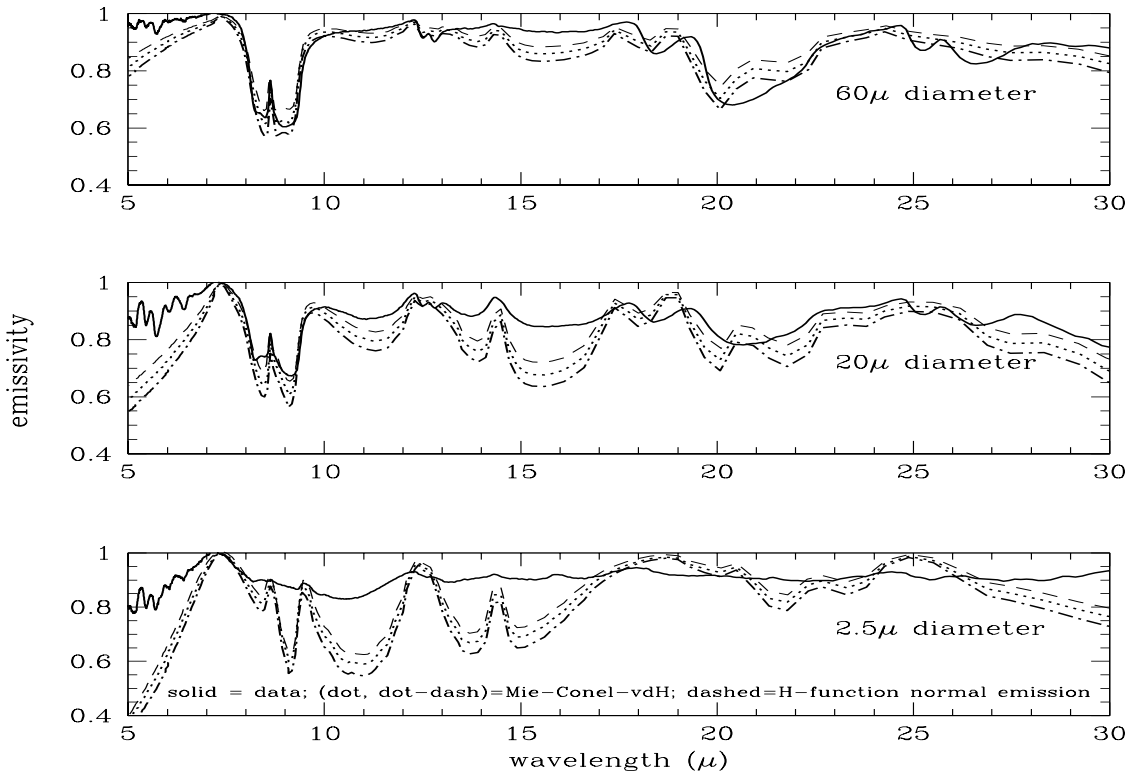

Fig. 1. Comparison of Mie-Conel, Mie-van De Hulst, and Mie-H-function models (dotted, dot-dashed, and dashed lines) with laboratory emissivity measurements of layers of size-sorted granular quartz (solid lines, J. Michalski and P. Christensen, personal communication, 2006), for three separate grain sizes

For the largest grain sizes, our models, and previous models, are in fair agreement with the experimental data. However, for wavelength-sized and smaller grains, the correspondence is unsatisfactory, as already shown by Moersch and Christensen (1995, MC95), Mustard and

Hays (1997; MH97), and Pitman et al (2005) for grains with a well known size distribution. For quartz, MH97 and MC95 both find that strong restrahlen bands show almost no variation with regolith grain size while the data show noticeable variation. These are the high-refractive-index "surface scattering" regimes. Even bigger discrepancies are seen in the "volume scattering" transparency regimes. For moderate-size grains, the models predict emissivity minima in transparency bands such as 10-12μm, 13-14.5μm, and 15-17μm,which are much more dramatic than shown by the data, and the discrepancy increases with smaller grain size (also pointed out by Wald and Salisbury 1995). MH97 even show (in their figure 11) that the sense of the observed 10-12 and 13-14μm band strength variation, as grain size varies between 2-25μm, is *directly opposite* the sense predicted by the models in figure 1. In the spectral range 19-22.5μm, the models predict a double minimum in the emissivity while the data show a single minimum. This might be related in some way to how all these models treat the birefringence properties of SiO_2. Furthermore, MH97 show that the asymmetry of the restrahlen bands for Olivine at 9-11μm wavelength is opposite that of theoretical predictions. For SiO_2, our model results reinforce these conclusions. Hapke (2008) suggested that, for almost all cases except extremely high grain albedos, increased (realistic) volume filling factor *increases* reflectivity. However, as we see from comparing ideal models to nonideal data, the data show increased *emissivity* (decreased reflectivity) in transparency regions relative to the models. As we show models which both include, and reject, grain forward scattering, this alone is unlikely to be the primary reason (although the $H-$function model, which rejects forward scattering and forces the phase function to be isotropic, might be said to provide marginally better agreement with the data). Thus, we feel that a good explanation for the observed effects is still to be found.

It is perhaps not surprising that current models have such problems, because their basic assumptions (widely spaced and independently scattering particles which are either spherical (Mie), much larger than the wavelength, and/or independently scattering are violated by key physical properties of regolith surfaces in the regime shown (close packing, irregular particles, wavelength size grains). The fact that these popular models fail to capture important features of laboratory silicate data casts doubt on their validity for inferences of grain composition or size from mid-infrared observations of planetary surfaces in general. As discussed below, we suspect the primary explanation for the discrepancy is the effect of the nonideal (moderate to large) volume filling factor of the real granular material.

3. A new RRT model using the Discrete Dipole Approximation

Our model is based on the Discrete Dipole Approximation (DDA) which calculates the scattering and absorption of electromagnetic waves by a target object of arbitrary structure - in our case, for closely packed, irregular grains of arbitrary radius r_g. Target objects are mod-

eled with a suitably populated lattice of individual polarizable dipoles with size smaller than a wavelength. The polarizability of each dipole can be adjusted to represent the refractive index of an arbitrary material or free space (Draine and Flatau 1994,1988). An important criterion for the dipole lattice is that the size of, and spacing between, the dipoles (both given by d) must be small compared with the wavelength $\lambda = 2\pi/k$ of the incident radiation in the target material: $|M|kd < 1/2$, where M is the complex refractive index of the target. The second criterion is that for a given d, the total number of dipoles N must be large enough to resolve the internal structure of the target and its constituent monomers satisfactorily. In our case, monomers may overlap, but typically we need $(r_g/d)^3$ dipoles per monomer. Heterogeneous composition and irregular shape of monomers are easily captured this way, but we reserve those refinements for the future.

To apply the DDA approach to a regolith layer, we have made several changes from the traditional implementation. In one novel modification, horizontally extended, semi-infinite slabs of regolith, made up of closely packed grains of arbitrary size and shape, are modeled using a single target "unit cell" subject to periodic horizontal boundary conditions or *PBC* (Draine and Flatau 2008). In a second novel modification, the emergent intensities from the layer are calculated using the full near field solution; traditionally all scattering calculations have been done in the far field. This step itself has two parts: evaluating the scattered electric field on a planar 2-D grid close to the target cell, and evaluating the angular intensity distribution emerging from this grid in an outbound hemisphere using a Fourier transform approach. These angular distributions of emergent intensity, which can be sampled on Gaussian quadrature grids, can then provide input into standard adding-doubling codes to build up solutions for thicker layers than we can model directly with DDA; this next step is a subject for a future paper.

Below we describe our approach in its three main elements: (A) horizontal periodic boundary conditions, (B) calculation of the scattered fields in the near field of the target, and (C) determination of the angular distribution of the emitted radiation using a Fourier analysis "angular spectrum" method.

3.A. Periodic boundary conditions

A finite rectangular slab of monomers composed of gridded dipoles, referred to as the Target Unit Cell (TUC), is periodically replicated, to represent a horizontally semi-infinite 3-D layer (see Draine and Flatau 2008). Each dipole in the TUC has an image dipole in each periodic replica cell. All dipoles in the TUC and replica oscillate with the appropriate phases in their initial response to an incident plane wave. The electromagnetic field inside the target is then recalculated as the sum of the initial radiation and the field from all other dipoles in the layer; monomers on the edge of the TUC are still embedded in the field of many adjacent

monomers by virtue of the PBC. A steady state solution is obtained by iterating these steps. The dipoles are located at positions $\mathbf{r} = \mathbf{r}_{jmn}$ with the indices m, n running over the replica targets, and j running over the dipoles in the TUC:

$$\mathbf{r}_{jmn} = \mathbf{r}_{j00} + mL_y\hat{y} + nL_z\hat{z} \tag{7}$$

where L_y, L_z are the lengths of the TUC in each dimension. The incident E field is

$$\mathbf{E}_{inc} = \mathbf{E}_0 e^{ik\cdot\mathbf{r}-iwt}. \tag{8}$$

The initial polarizations of the image dipoles $\mathbf{P}_{jmn}$ are also driven by the incident field, merely phase shifted relative to the TUC dipole polarization $\mathbf{P}_{j00}$:

$$\mathbf{P}_{jmn} = \alpha_j \mathbf{E}_{inc}(r_j, t) = \alpha_j \mathbf{E}_0 e^{ik\cdot(\mathbf{r}_{j00}+mL_y\hat{y}+nL_z\hat{z})-iwt} = \mathbf{P}_{j00} e^{ik(\mathbf{r}_{jmn}-\mathbf{r}_{j00})} \tag{9}$$

The scattered field at position j in the TUC ($m = n = 0$) is due to all dipoles, both in the TUC (index l) and in the replica cells.

$$\mathbf{E}_{j00} = -\mathbf{A}_{j,lmn}\left[\mathbf{P}_{l00} e^{ik(\mathbf{r}_{jmn}-\mathbf{r}_{j00})}\right] = -\mathbf{A}_{j,lmn} e^{ik(\mathbf{r}_{jmn}-\mathbf{r}_{j00})}\mathbf{P}_{l00} \equiv -\mathbf{A}^{PBC}_{j,l}\mathbf{P}_{l00}. \tag{10}$$

$\mathbf{A}^{PBC}_{j,l}$ is a 3 x 3 matrix that defines the interaction of all dipoles in the TUC and replicas residing in the periodic layer (Draine 1994, 2008). Once the matrix $\mathbf{A}^{PBC}_{j,l}$ has been calculated, then the polarization $\mathbf{P}_{j00}$ for each dipole in the TUC can be calculated using an iterative technique:

$$\mathbf{P}_{j00} = \alpha_j \left[\mathbf{E}_{inc}(r_j) - \sum_l \mathbf{A}^{PBC}_{j,l}\mathbf{P}_{l00}\right], \tag{11}$$

where the criterion for convergence can be set by the user. In the next two subsections we will show how we go from the field sampled on a two dimensional grid parallel to the target layer, to a full three dimensional angular distribution in elevation and azimuth relative to the target layer normal.

3.B. Calculating radiation from the PBC dipole layer

Once a converged polarization has been obtained for all dipoles in the target layer, we can calculate the radiated field. For most purposes in the past, the radiated field was calculated in the far field of the target ($kr \gg 1$); however, this introduces edge effects inconsistent with a laterally infinite horizontal layer, since the radiation is calculated by summing over the radiated contributions only from a single TUC (see Appendix B). This problem would remain even if we were to include more image cells or a larger TUC; no matter how large the target, its finite size will be manifested in the far radiation field as an increasingly narrow diffraction-like feature. Another consideration supporting the use of the near field, is that we

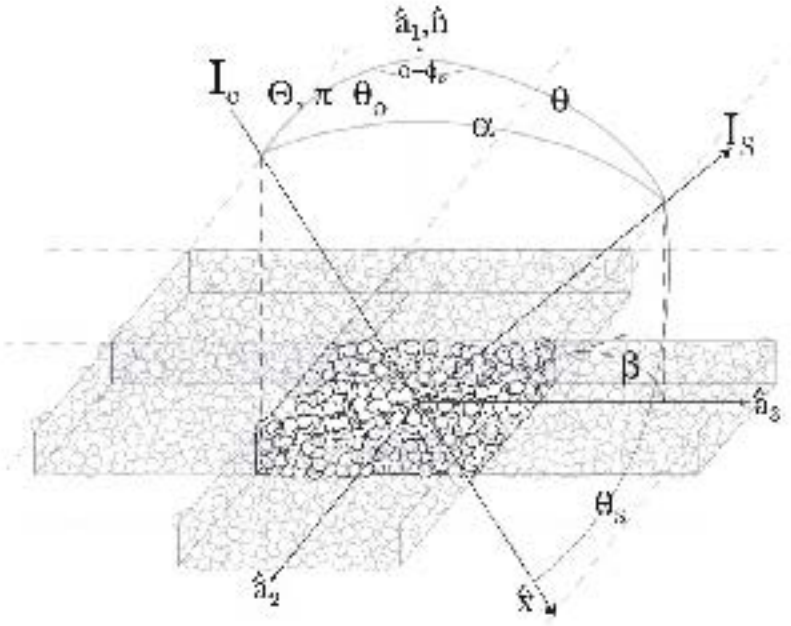

Fig. 2. Schematic of the DDA code operated in the Periodic Boundary Condition (PBC) regime, with the Target Unit Cell (TUC) shown in the center and image cells arrayed around. I_o indicates an incident plane wave (flux in erg cm^{-2} sec^{-1}) and I_s indicates the scattered flux. Θ (and θ) are the angles between the incident (and scattered) beam and the $\mathbf{a}_1$ axis normal to the particle layer. Also, ϕ_o and ϕ are the azimuth angles of these beams around the normal of the layer. The angle β determines the azimuth angle of the incident beam relative to the $\mathbf{a}_3$ axis fixed to the target. The phase angle of the scattered beam is α and the scattering angle of the emergent beam, relative to the incident beam, is θ_s.

plan to build up the properties of thick targets, beyond the computational limits of the DDA, by combining the properties of our DDA targets using an adding-doubling approach in which each is envisioned to be emplaced immediately adjacent to the next. For this application, the far field limit does not apply and we have to move closer to the layer to sample the radiation field.

3.B.1. The near field

Our solution to the problems mentioned above is to calculate the radiated field in close proximity of the target that is, in its near field. In the forward direction, this region can be thought of as the shadow of the layer. We use the full free space Green's function, which incorporates all proximity effects, to calculate the radiated field in this regime. The radiated field is a sensitive function of position with respect to the layer. In the horizontal (y and z) directions, the phase of the field fluctuates rapidly. In the x direction, as the field travels away from the layer, it transitions from the true near field (where evanescent waves can be present) to the Fresnel zone where patches of dipoles within the target are oscillating coherently, and finally to the far field limit where the layer is seen as a finite target.

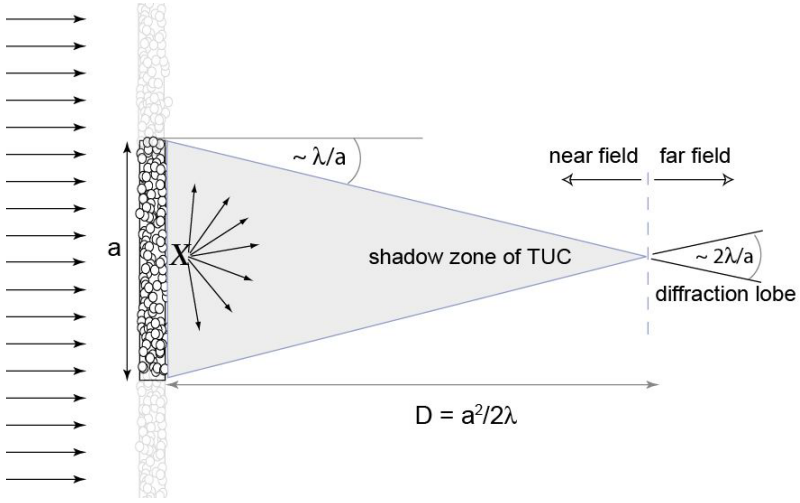

Fig. 3. Schematic of our approach, illustrating how we obtain the forward scattered diffuse intensity at point X in the shadow or Fresnel zone of the TUC, uncorrupted by edge effects from the TUC (see Appendix B). The diffuse reflectivity is determined at a similar distance from the lit face of the TUC.

3.B.2. Sampling the field on a 2-D sheet

The first step in obtaining the scattered intensity within the classical shadow zone of the slab is to calculate the total electric field on a 2-D grid (which we call the Target Unit Radiance or TUR) just outside the layer. We will use both the TUC and the image cells out to some distance in calculating the field on the TUR. The general expression for the field due to a collection of j dipoles with polarization $\mathbf{P}_j$ is as follows:

$$\mathbf{E}_{TUR} = k^2 \sum_{j=1}^{N} \mathbf{P_j} \cdot \vec{\vec{\mathbf{G}}}, \text{where} \tag{12}$$

$$\vec{\vec{\mathbf{G}}} = \frac{e^{ikr_{jk}}}{r_{jk}} \quad k^2(\hat{r}_{jk}\hat{r}_{jk} - \vec{\vec{\mathbf{I}}}) + \frac{ikr_{jk}-1}{r_{jk}^2}(3\hat{r}_{jk}\hat{r}_{jk} - \vec{\vec{\mathbf{I}}}) \quad , \tag{13}$$

where r_j = distance to grid points in the TUC, r_k = distance to grid points in the TUR, $r_{jk} = |\vec{r}_j - \vec{r}_k|$, $\hat{r}_{jk} = (\vec{r}_j - \vec{r}_k)/r_{jk}$, $\vec{\vec{\mathbf{I}}}$ is the identity tensor, and $\vec{\vec{\mathbf{G}}}$ is the free space tensor Green's function. The field is calculated on TUR's on both sides of the slab, *i.e.*, on the reflected and transmitted sides. The transmitted side includes both the directly transmitted incident electric field that has been attenuated through the slab and the scattered field. This method has been written as a FORTRAN code called DDFIELD, one version of which is currently distributed with DDSCAT as a subroutine *(http://www.astro.princeton.edu/ draine/DDSCAT.html)*. The version used in this paper is slightly different and was parallelized using MPI and OpenMP. The dipole polarizabilities calculated by DDSCAT are fed into DDFIELD to calculate the electric field from them. The vector field $\mathbf{E}(y,z) = E_x(y,z)\hat{x} + E_y(y,z)\hat{y} + E_z(y,z)\hat{z}$, is calculated separately for each of the two polarization states of the incident radiation.

3.C. Determining the angular distribution of scattered intensity

Our approach to determining the emergent intensities in the near field, as a function of angle (θ, ϕ) for any given (θ_o, ϕ_o), follows the formalism of Mandel and Wolf (1994). A complex field distribution or waveform can be represented by a superposition of simple plane waves and Fourier decomposed across a plane (see below). The waveforms spatial frequency components represent plane waves traveling away from the plane in various angular directions. Consider a monochromatic wave-field $\mathbf{E}(x,y,z)$ that satisfies the Helmholtz equation across the TUR plane at $x = x_0$; it can be represented by a Fourier integral:

$$\mathbf{E}_{TUR} = \mathbf{E}(x_0; y, z) = \int\int \mathbf{E}(x_0; k_y, k_z) e^{i(k_y y + k_z z)} dk_y dk_z. \tag{14}$$

Then the field $\mathbf{E}(x_0; y, z)$ has the following inverse transform :

$$\mathbf{E}(x_0; k_y, k_z) = \int\int \mathbf{E}(x_0; y, z) e^{-i(k_y y + k_z z)} dy dz. \tag{15}$$

The Helmholtz equation is:

$$(\bigtriangledown^2 + k^2)\mathbf{E}(\mathbf{r}) = 0, \text{where } \mathbf{r} = (x, y, z). \tag{16}$$

Substituting the 2-D representation of the field $\mathbf{E}(x, y, z)$ into the Helmholtz equation, we get the differential equation:

$$\frac{\partial^2 \mathbf{E}(x_0; y, z)}{\partial x^2} + k_x^2 \mathbf{E}(x_0; y, z) = 0 \tag{17}$$

with the general solution:

$$\mathbf{E}(x_0; k_y, k_z) = A(k_y, k_z)e^{ik_x x_0} + B(k_y, k_z)e^{-ik_x x_0}. \tag{18}$$

In addition we assume

$$k_x^2 = k^2 - k_y^2 - k_z^2, \quad k = \frac{2\pi}{\lambda} \tag{19}$$

$$k_x = (k^2 - k_y^2 - k_z^2)^{\frac{1}{2}} \text{ where } k_y^2 + k_z^2 \leq k^2, \text{ or} \tag{20}$$

$$k_x = i(k_y^2 + k_z^2 - k^2)^{\frac{1}{2}}, \text{ where } k_y^2 + k_z^2 > k^2 \tag{21}$$

Because the roots with $k_y^2 + k_z^2 > k^2$ are evanescent and will decay rapidly away from the layer, we will sample the field at a position x_0 where the evanescent terms have decayed and are negligible (as determined by tests). We would like to compute the scattered field emanating away from the target, therefore we will only consider the solution in a half space: in the reflected region $x < 0$, $B(k_y, k_z) = 0$ (equation 18) and in the transmitted region $x > 0$, $A(k_y, k_z) = 0$. We can proceed with the development using one side since the other differs by a minus sign. For example on the transmitted side we can write the Fourier transform of the electric field across any plane $x = x_0$ as follows:

$$\mathbf{A}(k_y, k_z)e^{ik_x x_0} = \qquad \mathbf{E}(x_0; y, z)e^{i(k_y y + k_z z)} dk_y dk_z \tag{22}$$

where the scattered electric field $\mathbf{E}(x_0; y, z)$ has been computed on a grid of points on a plane $x = x_0$ in the shadow zone (the TUR). The Fourier transform of the electric field on the TUR gives the relative strength of each spatial frequency component $\mathbf{A}(k_y, k_z)$ composing that field, and therefore of each plane wave stream leaving the TUR. The distribution of energy as a function of spatial frequency $k = 2\pi/\lambda$ should be highly localized at k^2, allowing us to determine $k_x^2 = k^2 - k_y^2 - k_z^2$. Its angular distribution is the angular distribution of the emergent scattered intensity at the plane $x = x_0$. Because the components $\mathbf{A}(k_y, k_z)$ are formally fluxes, we must transform them into intensities (see section 3.C.1). This approach will also provide a way to discriminate against any static components in the field; appearance of significant anomalous energy at high spatial frequencies (*i.e.* much higher than $|\vec{k}|$), is an indication of static, evanescent fields. If this problem were to appear (it has not yet, with $x_0 \sim \lambda$), we would merely move the TUR slightly further from the face of the TUC.

3.C.1. Flux and Intensity

The discrete transform quantities $A_i(k_y, k_x)$ with $i = x, y, z$ represent components of plane waves with some unpolarized, total flux density

$$\sum_{i=x,y,z} |A_i(\theta, \phi)|^2 \tag{23}$$

propagating in the directions $\theta(k_y, k_z), \phi(k_y, k_z)$, where the angles of the emergent rays are defined relative to the normal to the target layer and the incident ray direction (θ_0, ϕ_0):

$$k_x = k\cos\theta \tag{24}$$

$$k_y = k\sin\theta\sin(\phi - \phi_0) \tag{25}$$

$$k_z = k\sin\theta\cos(\phi - \phi_0) \tag{26}$$

where $k = 1/\lambda$ and we solve at each (k_y, k_z) for $k_x = (k^2 - k_y^2 - k_z^2)^{1/2}$. It is thus an implicit assumption that all propagating waves have wavenumber $k = 1/\lambda$; we have verified numerically that there is no energy at wavenumbers $> k$, as might occur if the the DDFIELD sampling layer at x_o had been placed too close to the scattering layer.

From this point on, we assume fluxes are summed over their components i and suppress the subscript i. The next step is converting the angular distribution of plane waves, or flux densities (energy/time/area), $|A(k_y, k_z)|^2$ into intensities (energy/time/area/solid angle). Perhaps the most straightforward approach is to determine the element of solid angle subtended by each grid cell $dk_y dk_z$ at (k_y, k_z): $d\Omega(\theta, \phi) = \sin\theta(k_y, k_z) d\theta(k_y, k_z) d\phi(k_y, k_z)$. Then the intensity is

$$I(\theta, \phi) = |A(k_y, k_z)|^2 / d\Omega(\theta, \phi) = |A(k_y, k_z)|^2 / d\Omega(k_y, k_z). \tag{27}$$

We have computed the elemental solid angles in two separate ways. One obvious but cumbersome way to calculate $d\Omega(k_y, k_z)$ is to determine the elemental angles subtended by each side of the differential volume element using dot products between the vectors representing the grid points, and multiply them to get the element of solid angle $d\Omega(k_y, k_z)$. Another method makes use of vector geometry to break $d\Omega(k_y, k_z)$ into spherical triangles (Van Oosterom and Strackee 1983). These methods agree to within the expected error of either technique. A simpler and more elegant approach is to rewrite equation 27 as

$$I(\theta, \phi) = \frac{|A(k_y, k_z)|^2}{dk_y dk_z} \frac{dk_y dk_z}{d\Omega(k_y, k_z)} = \left(\frac{|A(k_y, k_z)|^2}{(1/L)^2}\right) \frac{\mathcal{J} d\theta d\phi}{d\Omega(k_y, k_z)}, \tag{28}$$

where we use standard Fourier relations to set $dk_y = dk_z = 1/L$ (see Appendix C), and the Jacobian $\mathcal{J}$ relates $dk_y dk_z = \mathcal{J} d\theta d\phi$:

$$\mathcal{J} = (\partial k_y/\partial\theta)(\partial k_z/\partial\phi) - (\partial k_y/\partial\phi)(\partial k_z/\partial\theta) \tag{29}$$

Then from equations (27-29) above *do you mean (25 - 26)* , $\mathcal{J} = k^2\sin(\theta)\cos(\theta)$, and

$$I(\theta,\phi) = \frac{|A(k_y,k_z)|^2(kL)^2\sin(\theta)\cos(\theta)d\theta d\phi}{\sin(\theta)d\theta d\phi} \tag{30}$$

$$= |A(k_y,k_z)|^2\cos(\theta)(kL)^2 = |A(k_y,k_z)|^2\cos(\theta)(L/\lambda)^2. \tag{31}$$

The above equations 27 - 31 demonstrate that $d\Omega = \sin\theta d\theta d\phi = \sin\theta(dk_y dk_z/\mathcal{J}) = \sin\theta(1/L^2)/k^2\sin\theta cos\theta = \lambda^2/(L^2\cos\theta)$. Numerical tests confirm that this expression reproduces the directly determined elemental solid angles, so we will use this simple closed-form relationship.

After checking the region of k-space $k_y^2 + k_z^2 > k^2$ for nonphysical, anomalous power and thereby validating the location x_0 of the sampled $E(x_0; y, z)$, and converting to intensity as described above, the Cartesian grid of $I(k_y, k_z)$ is splined into a polar grid $I(\mu_i, \phi_j)$ with coordinate values μ_i given by the cosines of Gauss quadrature points in zenith angle from the layer normal. This splining is designed to eliminate the nonphysical region $k_y^2 + k_z^2 > k^2$ from further consideration, and streamline subsequent steps which will use Gaussian quadrature for angular integrations of the intensities.

The radiation on the forward-scattered side of the layer is all-inclusive - that is, includes both the scattered radiation and the radiation which has not interacted with any particles (the so-called "directly transmitted beam"). We obtain the intensity of the directly transmitted beam after correcting for the smoothly varying, diffusely transmitted background, allowing for the finite angular resolution of the technique, and from it, determine the effective optical depth τ of the target layer including all nonideal effects (see section 6). For subsequent applications involving the adding/doubling techniques (not pursued in this paper), the attenuation of the direct beam through each layer with the same properties will simply scale as $\exp(-\tau/\mu)$. No such complication afflicts the diffusely reflected radiation.

3.D. Summary

As described in section 3.B.2, subroutine DDFIELD is used to determine the electric field $E(x_0; y, z)$ on a 2D grid located a distance x_o away from the layer (equations 12 and 13). The sampling location x_0 is adjustable within the shadow zone (the near field of the layer), but should not be so close to the target as to improperly sample evanescent or non-propagating field components from individual grains. Incident wave polarizations can be either parallel or perpendicular to the scattering plane (the plane containing the mean surface normal $\mathbf{e}_x$ and the incident beam). At each incident zenith angle θ_0, calculations of $E(x_0; y, z)$ are made for many azimuthal orientations, (defined by the angle β) and in addition, calculations are made for several regolith particle realizations (rearrangement of monomer configurations). All scattered intensities are averaged incoherently. Such averaged intensities $I(\theta_0, \theta, \phi - \phi_0)$ can then be obtained for a number of incident zenith angles θ_0, and determine the full diffuse

scattering function $S(\tau;\mu_0,\mu,\phi-\phi_0)$ and diffuse transmission function $T(\tau;\mu_0,\mu,\phi-\phi_0)$ of a layer with optical depth τ and emission angle $\mu = cos\theta$, for use in adding-doubling techniques to build up thicker layers if desired. As noted by Hansen (1969) the quantities $S(\tau;\mu_0,\mu,\phi-\phi_0)$ and $T(\tau;\mu_0,\mu,\phi-\phi_0)$ can be thought of as suitably normalized intensities; thus our fundamental goal is to determine the intensities diffusely scattered and transmitted by our layer of grains. For the proof of concept purposes of this paper, it is valuable to have both the reflected and transmitted intensities for layers of finite optical depth. We further average the results for $I(\theta_0,\theta,\phi-\phi_0)$ over $(\phi-\phi_0)$ to reduce noise, obtaining zenith angle profiles of scattered intensity $I(\theta_0,\theta)$ for comparison with profiles obtained using classical techniques (section 5).

4. Dielectric slab tests

The simplest test of our DDA model is simulating a uniform dielectric slab having refractive index $M = n_r + in_i$, which has well known analytical solutions for reflection and transmission given by the Fresnel coefficients. This slab test can be applied to both parts of our model: the electric field calculated on the TUR directly from dipole polarizabilities (using DDFIELD, section 2.2) can be compared to Fresnel reflection and transmission coefficients, and the Angular Spectrum technique (section 2.3), with all its associated conversions, can also be tested by comparing the position and amplitude of the specular directional beam on the reflected and/or transmitted sides of the slab with Fresnel's coefficients and Snell's law.

We used the DDA with PBC to simulate a slightly absorbing homogeneous dielectric slab with $M = 1.5 + 0.02i$. The slab consists of 20x2x2 dipoles along its x, y, and z dimensions and is illuminated at $\theta_0 = 40°$. Figure 4 compares the amplitude of the electric field on our TUR grid, on both the transmitted and reflected sides of the slab, with Fresnel's analytical formulae for the same dielectric layer. The dimensions of the slab are held constant while the wavelength is varied, resulting in the characteristic sinusoidal pattern in reflection as internal reflections interfere to different degrees, depending on the ratio of slab thickness to internal wavelength. Transmission decays with increasing path length because of the small imaginary index.

The results of figure 4 are orientationally averaged; the results for individual azimuthal orientations β (not shown) contain a four-fold azimuthally symmetric variation of the electric field, with respect to the slab, which we expect is an artifact of slight non-convergence in the layer. The variation is smooth and less than the ten percent in magnitude, and when our granular layer calculations are averaged over many (typically 40) values of the azimuthal angle β (see figure 2) it becomes negligible.

To test the Angular Spectrum approach to getting the magnitude and angular distribution of scattered radiation (section 3.C and Appendix), we next analyzed the location and strength

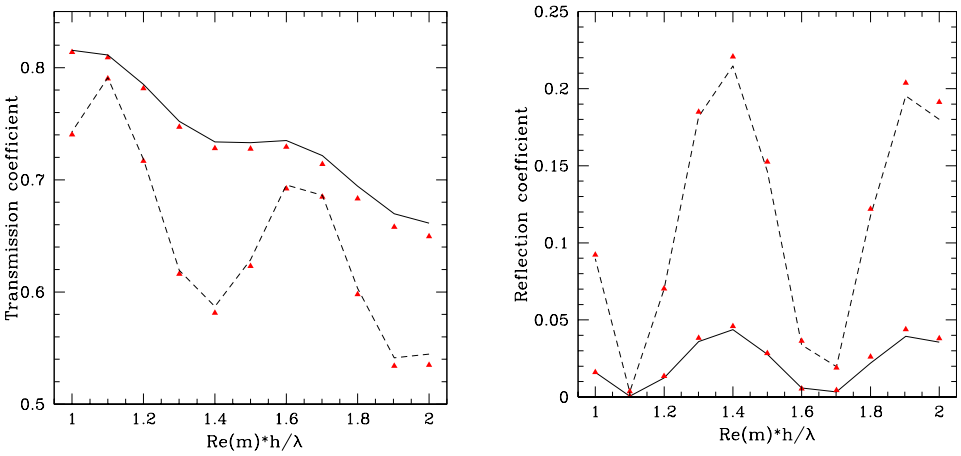

Fig. 4. Left: The transmission coefficient for a slightly absorbing dielectric slab as a function of wavelength, for two different planes of polarization. The red triangles show the square of the electric field amplitude calculated on the TUR by DDFIELD, and the solid and dashed lines ($\parallel$ and $\perp$ or TE and TM modes respectively) are the Fresnel intensity coefficients for the same slab in orthogonal polarizations. The slab is h =20 dipoles (6 μm) thick with an index of refraction $M = 1.5 + 0.02i$, and the wavelength λ varies between 4.5-9μm (see section 3.2). Right: Comparison of the Fresnel reflection coefficients for the same slab (lines) with square of the electric field amplitude as calculated by DDFIELD (triangles) on the TUR on the opposite side of the TUC.

of the specular beam on either side of the layer. We sampled the electric field vector on the 2-D TUR grid of points, with $N_y = N_z = 64$, and took the Fourier transform of the vector field separately for each coordinate (x, y, z). The power was obtained by squaring the transformed amplitudes from each coordinate (equation 23). Contour plots of scattered intensity (figure 5) show the specular peak of the reflected intensity for various incident angles, along with a diffraction pattern at the 1% level resulting from the square (unwindowed) TUR aperture. We can see that as we change the incidence angle, the emergent specular beam changes location in k-space (θ, ϕ space) appropriately, confirming that our model is consistent with Snell's law. We also verified that the magnitude of the flux density - the intensity integrated over the specular peak - is equal to the power $|E_o^2|$ in the E field on the TUR (which also

matches the Fresnel coefficients).

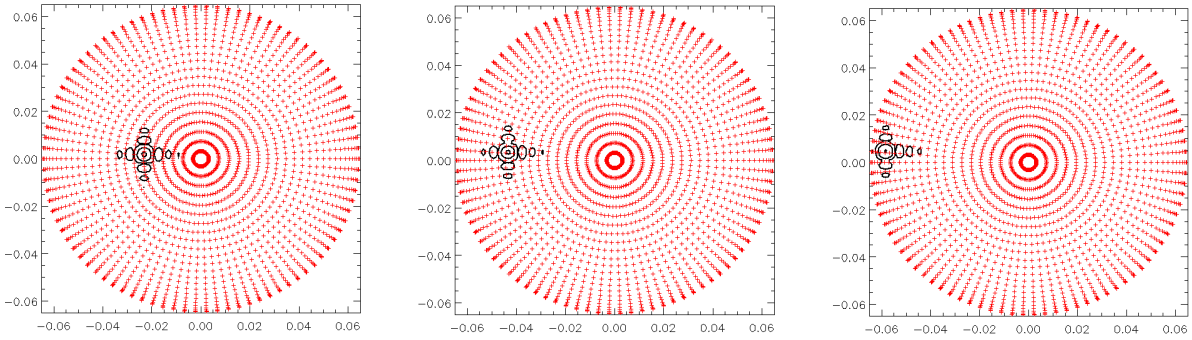

Fig. 5. Specular reflection from a dielectric slab, from the output of our angular spectrum approach, shown in spatial frequency or k-space with axes (k_y, k_z), and overlain with red symbols (in the online version) indicating the grid of (θ, ϕ) onto which we spline our output intensities. The results are shown for for three incident radiation angles: $\theta_o = 20°$, $40°$, and $60°$. The emergent beam, shown as black contours, moves in k-space at the correct emergent angle for specular reflection. The lowest contours, at the level of 1% of the peak in all three cases, show the sidelobes arising from Fourier transforming our square TUR.

We then assessed the effect of dipole scale resolution using the dielectric slab. Since the PBC calculations are computationally challenging (requiring multiple processors and days to reach convergence) we were encouraged to use the most relaxed $|M|kd$ criterion to reduce computation time while exploring a range of variations in packing density, over a number of target realizations and orientations. Traditionally it is assumed that the grid dipole size d must result in $|M|kd \leq 0.5$ to get acceptable convergence (Draine and Flatau 1994). To explore this further, we looked at the variation of the electric field reflected and transmitted by a dielectric slab with various $|M|kd$ values ranging between 0.4-1.0. In figure 6 we can see that the field variation and its comparison with Fresnel's coefficients is in acceptable agreement (within less than 20% in the worst case) for $|M|kd$ values below 0.8 and diverges from there. Further tests are discussed below, using actual granular layers. In this first paper we have pushed the envelope somewhat, to complete more cases at an exploratory level, so do not claim accuracy better than 15% on average, but have never exceeded $|M|kd = 0.8$. Clearly, for future applications, it is always good to increase resolution to achieve better accuracy when quantitative results are of importance.

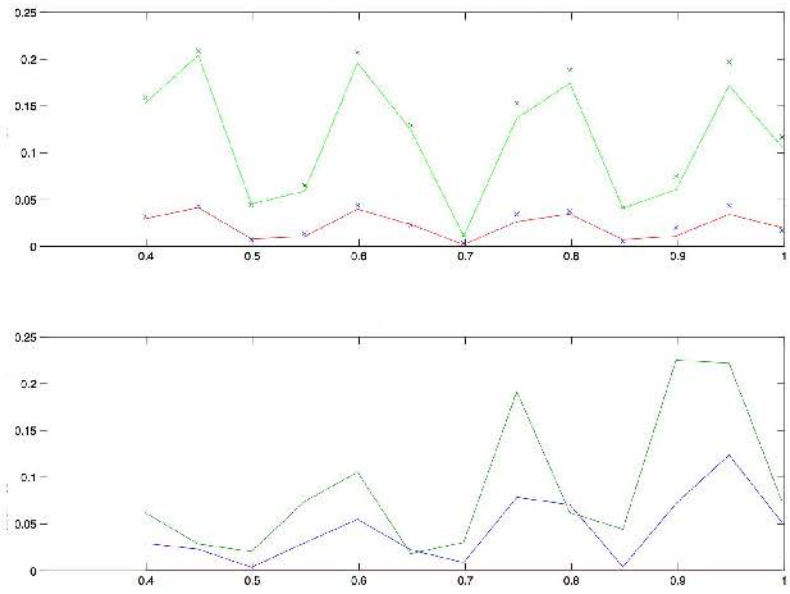

Fig. 6. Tests of the code resolution, defined by the product $|M|kd$, normally said to require $|M|kd \leq 0.5$. Top: Reflectivity in orthogonal polarizations from a dielectric layer for various $|M|kd$ values ranging between 0.4-0.9 compared with Fresnel's analytical solution. Bottom: The percent difference between Fresnel's coefficient and the dielectric slab reflectivity.

5. Granular layers

Here we introduce granular layers, which produce more complex, diffusely scattered intensity distributions. For this first study we took the simplest approach to generating granular layers by populating the TUC with spherical monomers of the same size and composition which may overlap, as distinguished from a "hard sphere" approach where spherical monomers can only touch (*eg.* Scarnato et al. 2012). Our primary motivation for this choice, at this stage, is better control over the porosity or filling factor of the granular target. The most dense granular TUC's we have studied have a filling factor of 77%. Because the monomer size is comparable to the wavelength, our working limit of roughly several million dipoles is reached with dense targets that are about five monomers deep and 6-7 monomers across, making up a TUC box with several hundred monomers (assuming $|M|kd = 0.8$) and a few thousand dipoles per monomer. For comparison, figure 7 shows the dense target (essentially a solid with internal voids, because of the extensive overlap of nominally spherical monomers) as well as a target of more moderate porosity, having filling factor of 20%. In the more porous target,

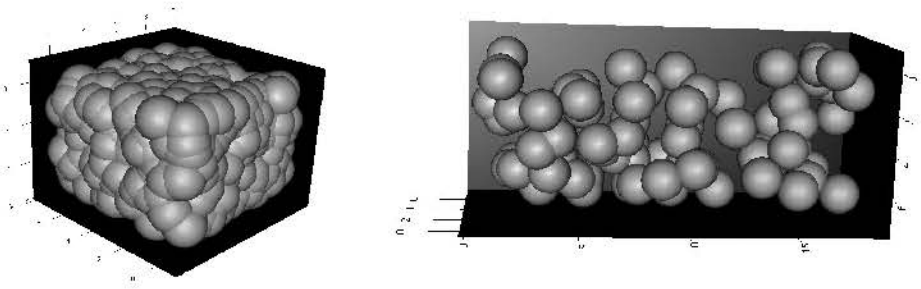

Fig. 7. Two of our granular target Unit Cells (TUCs). Left: Granular TUC constructed by overlapping monomers with 77% packing fraction; Right: Granular TUC with 20% packing fraction; the long axis is L_x. The grid in the 77% case is roughly 100 dipoles on a side so the monomers are each composed of approximately 4000 dipoles.

the same number of active dipoles (dipoles representing scattering material) is contained in a larger and deeper TUC. We have found that memory limitations per processor on typical massively parallel systems (such as the Altix at Ames Research Center that we used for this study) restrict the maximum volume of the TUC, regardless of the number of active dipoles, and we typically expand or contract the maximum dimension (remaining within tolerable limits) to generate targets of variable filling factor while maintaining the same number of monomers, to keep the effective optical depth of the target constant while porosity is varied. The periodic boundary conditions mirror the target in its smaller dimensions; our target is less like a pizza box than a brick standing on end.

As before, the scattered field $I(\theta, \phi)$ from each target is calculated for each combination of incident polarization and azimuth orientation β, and averaged incoherently for each polarization over azimuth angle ϕ to get an intensity profile as a function of zenith angle θ for a given orientation β, which are then averaged to get a single $I(\theta)$ profile. We selected SiO_2 as our target material, because several of the best constrained laboratory studies, with careful determination of grain size distributions, used SiO_2 grains (see section 2). We use quartz refractive indices from Wenrich and Christensen (1996) for these monomers at 15.5μ wavelength, which is in the middle of the deepest "transparency band" (all the transparency bands are problematic for current models as discussed in section 2 and shown in figure 1). In all granular cases so far we assumed an incident beam at incidence angle $\theta_0 = 40°$.

5.A. Granular layer tests at high and moderate porosity

For granular layers, we first assess varying dipole resolution and different target realization (a new realization is an independent configuration of randomly placed monomers, having

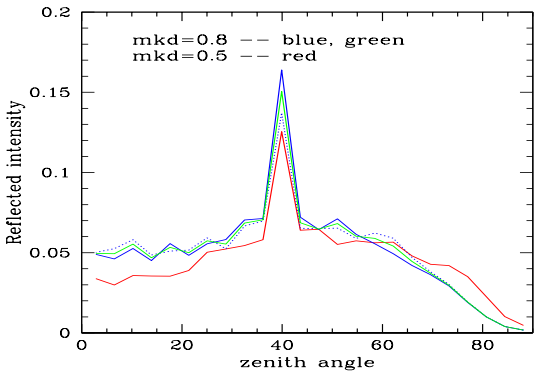

Fig. 8. *replot this vs sin(zenith angle) and check units on vertical axis* Reflected intensities for two realizations (solid and dotted blue, with the average of the two in green) of a granular layer with 77% filling factor and $|M|kd = 0.8$. The averaged intensity for one of the realizations, but using $|M|kd = 0.5$, is shown in red for comparison. Variations due to different realizations are small (at least for this dense target) and variations with $|M|kd$ are within an acceptable limit for our initial studies, in which we will not study detailed variations in the shape of these profiles but only their overall level and trends (see section 6).

the same overall porosity). Averages over β orientations and orthogonal polarizations are, as always, done incoherently, and additional averages over scattering azimuthal angle $\phi - \phi_0$ are taken to produce plots of intensities as a function of emission angle θ (viewing angle from layer normal). In related tests (not shown) we also compared averaging in k-space, prior to splining our intensity results onto grids of (θ, ϕ); it turned out that the profiles were more repeatable and smoother done after splining and averaging in azimuth.

Two cases of the the same target realization of the dense target (77% filling factor), but processed with different resolutions of $|M|kd = 0.5$ and $|M|kd = 0.8$, and one case for a second realization, are shown in figure 8. The scattered field has a continuous diffuse component as opposed to the flat dielectric slab's single specular peak, due to the granular structure in the layer. There is a remnant of the 40° specular peak visible in these cases because the granular TUC is almost dense and smooth enough to be a solid surface (see figure 7). Figure 8 shows that the scattered intensity varies by about 10% between the two $|M|kd$

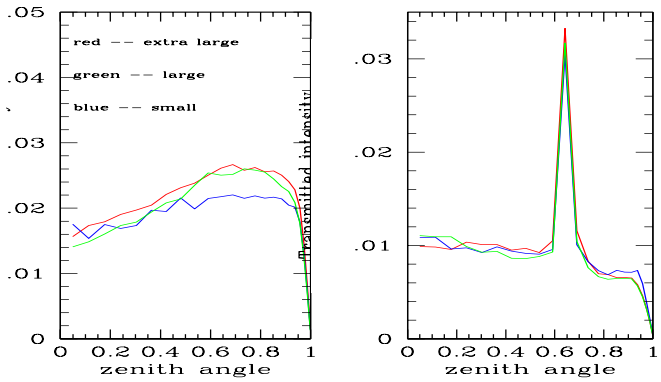

Fig. 9. Reflected (left) and transmitted (right) intensity as a function of zenith angle for 0.2 filling factor granular layer targets of various sizes. Note the appearance of the directly transmitted beam $I_o exp(-\tau/\mu_o$ (see text). Convergence is excellent for the *provide specific dimensions for the three target sizes and relabel x axis.*

cases, and the two realizations with the same resolution agree even better. We expect that our more sparse targets will require more realizations to achieve this level of convergence, because of their higher entropy in a sense. The effects of the somewhat lower resolution than ideal ($|M|kd = 0.8$) are quantitatively discernible but not qualitatively significant, and consistent with our uncertainty goals for this first paper.

We also assessed the convergence associated with the lateral size of the TUC (L_y, L_z) by comparing the reflected and transmitted intensities from various TUC sizes. As shown in figure 9, the intensities calculated using targets of several (transverse) sizes are adequately size convergent at the level of accuracy we have decided to tolerate for this first study, so we will generally use the smallest TUC to speed up our calculations.

Note that figure 9 shows how the directly transmitted beam appears in our DDA modeling (it is inextricably part of the field on the transmission side of the target). The amplitude of the directly transmitted beam decreases, of course, as the optical depth of the layer increases (see more discussion of this below and in section 6), and a similar-looking contribution from a *diffusely* transmitted, forward-scattered lobe becomes more possible. Particle sizes in question are too small to produce a forward-scattering lobe as narrow as the directly transmitted beam seen in figure 9 and similar figures in this paper, for wavelength-grain combinations treated

here. We can use the amplitude of the direct beam to determine the *actual* optical depth of the layer, and compare that with the value predicted by Mie theory extinction efficiency Q_e: $\tau = N\pi r^2 Q_e(r,\lambda)/L_y L_z$, where N is the number of monomers of radius r in the TUC, and its cross-sectional size is $L_y L_z$. We have not yet assessed in detail the degree to which porosity affects the classical dependence of extinction $\tau(\mu) = \tau_o/\mu$, where τ_o is the normal optical depth.

5.B. Granular layers: High porosity and comparison with classical models

An instructive experiment is to increase porosity until the monomers are far enough apart where they scatter independently, as verified by agreement with one of the classical solutions to the radiative transfer equation. It has been widely accepted that the independent scattering regime is reached when monomers are within three radii (most of these trace to an offhand statement in Van de Hulst 1957; see Appendix A also). This criterion was also discussed by Cuzzi et al (1980) and by Hapke (2008; see appendix A). Our initial results (discussed below) did not obviously confirm this criterion, so we ran an additional set at "ultra-low" porosity (*filling factor = 0.01* where we were certain it would be satisfied (see eg Edgar et al 2006)

For the classical model we used the facility code DISORT, which calculates the diffuse reflected and transmitted intensity at arbitrary angles, for a layer of arbitrary optical depth τ, given the phase function $P(\Theta)$ and single scattering albedo ϖ_o of the constituent scattering particles. In DISORT we use 40 angular streams and expand the phase function into 80 Legendre polynomials. We calculate $P(\Theta)$ and ϖ_o for our model grain population using Mie theory, assuming a Hansen-Hovenier size distribution with fractional width of 0.02. The mean monomer radius is exactly that of the DDA monomers for this case. Our Mie code has the capability to model irregular particles with the semi-empirical approach of Pollack and Cuzzi (1979), in which the phase function and area/volume ratio is modified somewhat, but that is not used at this stage and the particles are assumed to be near-spheres. No effort is made to truncate or remove any part of the phase function.

For the purpose of the present paper, we did not map out a fine grid of porosities to determine exactly where the independent scattering criterion is violated (see *eg.* Edgar et al 2006 for some hints). It is not implausible that this threshold will be some function of the ratio of grain size to wavelength (Hapke 2008) and a careful study of this is left for a future paper. For this paper our main goal is to get a final sanity check on the DDA code - to see that indeed it does properly manifest the scattering behavior of a low volume density ensemble of monomers, in the limit where we are confident this should be the case. Because memory limitations prevent us from simply expanding our 40-monomer targets to yet lower filling fraction, we constructed a different target, with only four monomers, keeping its dimensions

within the capabilities of the Altix (figure 10). The target construction initially allowed one or more monomers to be clipped by the planar edge of the TUC, needlessly complicating the scattering pattern, so we revised the target code and re-ran it with only four monomers and a volume filling factor of 0.01, the scattered light patterns are highly configuration-dependent, so we needed to run a number of realizations to achieve convergence in the scattered fields.

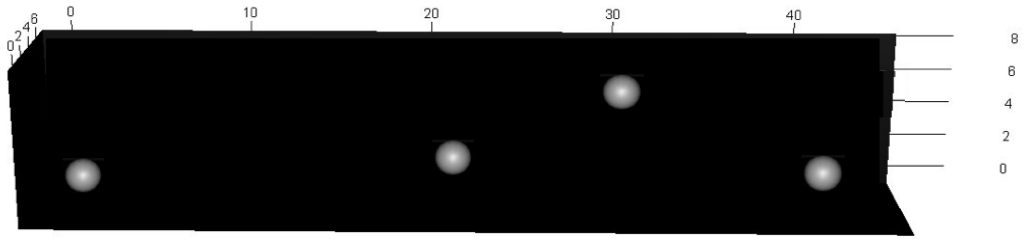

Fig. 10. A single realization of the ultraporous target. etc etc

Figure 11 shows a comparison of the diffusely reflected and transmitted fields at 15.5μm wavelength, averaged over azimuthal angle as before, for 20μm diameter SiO_2 monomers, compared with the DISORT predictions based on Mie albedos, extinction efficiencies, and phase functions for grains of these properties (but assuming a Hansen-Hovenier size distribution with width variance b=0.02). No correction was made for grain irregularity, but it is not implausible that something could be done, to allow for the fact that our monomers do not look as "spherical" as those in figure 7 but have raggedy edges due to the finite gridding. This figure averages intensities calculated from 1 realizations of the target.

Several interesting points may be made from figure 11. It is the first figure in which a direct comparison is made between DDA and "theoretical" diffuse transmissivities. The nominal diffraction pattern of our TUR, as viewed from off axis at 40°, is (not quite correctly) modeled by a simple $(\sin\theta/\theta)^2$ function because the mostly symmetric direct peak (see *eg* figure 5) is actually flattened by averaging on contours of constant θ. In comparing our DDA diffuse transmissivities with the DISORT values (which do not include the direct beam) we avoid regions that are plausibly contaminated by the sidelobes of the direct beam.

It is apparent that the diffusely reflected and transmitted intensities should and do increase towards grazing viewing angles in the actual case, as is seen in the DISORT results. Our intensities fail to match this behavior for zenith angles $\theta \to \pi/2$ because the summing of contributions from polarized dipoles into the TUR field, at a small distance above or below the target, only includes mirror cells out to a finite distance; thus intensities at truly grazing angles are not properly captured by the angular spectrum step. The same effect appears to varying degrees in diffuse intensities seen in figures 8 and 9 as well. As this is a known

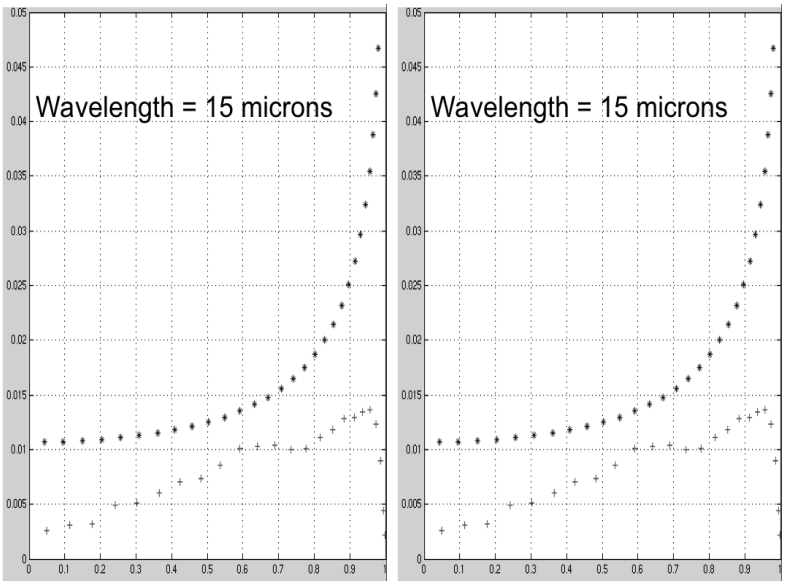

Fig. 11. Comparison of diffusely reflected (left) and transmitted (right) intensities from our ultrahigh porosity TUC (filling factor 0.01), with classical predictions for the nominal optical depth and monomer properties, using DISORT. The large peak in the transmitted intensity is the direct beam, broadened by our numerical resolution, for which an approximate analytical form (essentially $(\sin\theta/\theta)^2$) is overlain based on the dimensions of the TUR and the wavelength. The discrepancy between DDA and DISORT at large zenith angles is discussed in the text.

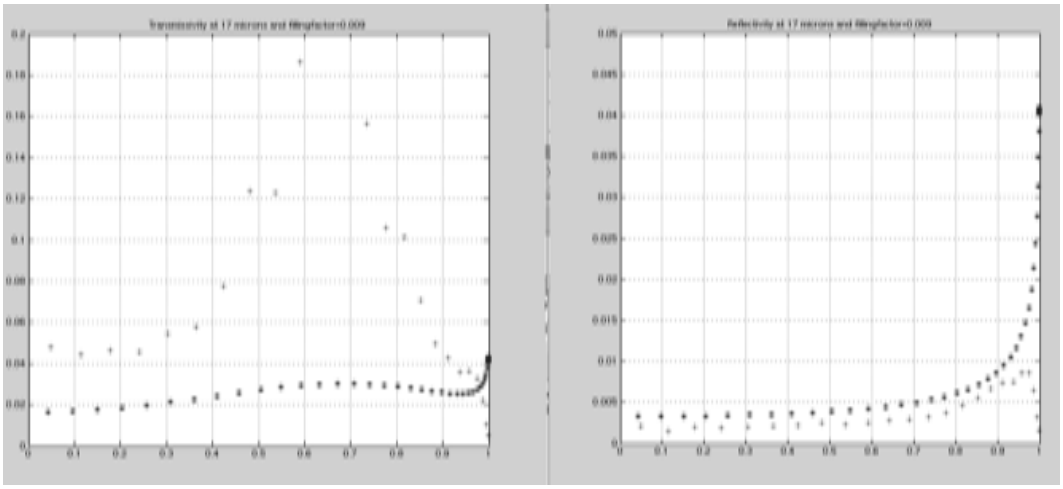

limitation of the model (correctable in principle given more computational time) we neglect these angular regions in assessing the fit of the DDA solution to the DISORT solution.

Overall it seems that the DDA/angular spectrum approach captures the appropriate diffuse reflected and transmitted intensity, using only the nominal particle albedo, extinction efficiency, and phase function calculated by Mie theory, when the porosity of the scattering volume is as low as 0.01 as here.

6. Results: Effects of increased packing density in granular layers

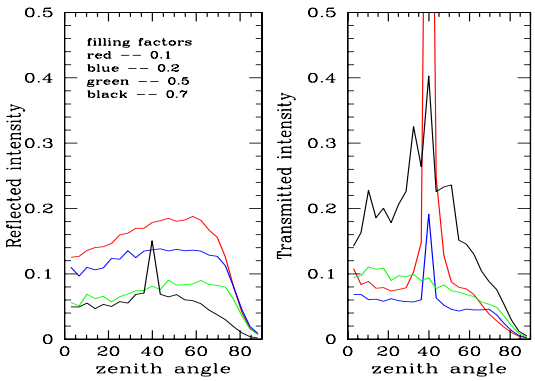

Fig. 12. Reflected and transmitted intensity as a function of zenith angle for granular layers of various filling factors. All layers are composed of 20μm diameter quartz monomers and illuminated at 15.5μ wavelength from 40° zenith angle. The more porous layers quickly lose the specular reflection shown by the densest layer, and have higher diffuse reflection and lower "diffuse" transmission, showing the direct beam as the expected narrow peak. The intensity of the "direct beam", and the diffuse transmissivity, shows a complex behavior (see text); for instance there is a transition porosity (50%; green curve) which shows no directly transmitted beam at all.

Starting with our densely packed TUC (filling factor 0.77; figure 7 left), we increased the depth of our TUC in the direction normal to the layer, merely expanding the monomer populations, to achieve successively lower filling factors of 0.50, 0.20 (figure 7), and 0.1. We calculate filling factors for these layers by taking the ratio of the number of quartz dipoles to vacuum dipoles in the TUC box. This is the range of porosities expected for planetary regoliths, for instance (P. Christensen, personal communication 2009). All these targets are modeled with the same amount of quartz material (the same size and number of monomers).

This way, we can isolate the effect of packing on the scattered intensity. For reference, the nominal optical depth of the most porous TUC, containing $N = 4$ SiO_2 monomers of radius r_g, is

$$\tau = NQ_{ext}\pi r_g^2/L_yL_z, \tag{32}$$

where $Q_{ext} = 3.7$ is the extinction coefficient at 15μm wavelength (from Mie theory) and the TUC has horizontal dimensions L_y and L_z, leading to a nominal value of $\tau \sim 0.2$.

The results are shown in figure 12. The dense layer (black curve) resembles a homogeneous dielectric layer with a slightly rough surface (it has a specular peak), and has the lowest diffuse reflectivity. The diffuse reflectivity increases monotonically with increasing porosity. This behavior is contrary to what is predicted (and often, but not always, seen) for layers of different porosity in the past (eg Hapke 2008, other refs), perhaps because previous models and observations tend to emphasize grain sizes much larger than the wavelength in question (we return to this below and in section 7).

The behavior in transmission is more complex, and not a monotonic function of porosity. For instance, the lowest filling factor (highest porosity) targets show a clear directly transmitted beam, the amplitude of which is consistent with the nominal optical depth of several. As porosity decreases, the intensity of the direct beam decreases even though the *nominal* optical depth of the target (equation 32) remains constant. This suggests that, in the sense of equation 32, Q_e is increasing with porosity. For porosity of 50%, the direct beam vanishes entirely. As porosity is decreased still further, a strong and broad pattern of "direct transmission" re-emerges.

We believe this behavior represents different regimes of forward propagation of the direct and diffusely transmitted radiation. For our highly porous layers where there are large vacuum gaps between monomers, the beam is extinguished as $I/I_o = exp(-\tau/\mu_o)$ where the optical depth $\tau = NQ_{ext}\pi r_g^2/L_yL_z$; Q_{ext} is the extinction coefficient, r_g is the radius of each monomer, and N/L_yL_z is the particle areal density defined as the number of particles per unit area of the layer. On the other hand, an electromagnetic beam traveling through a uniform, homogeneous dielectric layer is attenuated as $I/I_o = \exp(-4\pi n_i z/\lambda)$ where z is the path length and n_i is the imaginary refractive index. For the dielectric slab, this direct beam is augmented by multiply-internally-reflected waves, and the emergent beam is a combination of these leading to a delta function in the forward direction given by the Fresnel transmission coefficient. Our 77% filled target is not truly homogeneous, and has vacuum pockets with angled interfaces that deflect and scatter the forward-moving radiation into a broader beam or glare pattern. This physics determines the strength and general breadth of the forward-directed radiation seen in the black curve of figure 12 (right panel).

The case with 50% filling factor is an interesting transition region where, we believe, the monomers are closely packed enough to introduce interference effects and the vacuum gaps

are large and abundant enough to contribute to strong interface or phase shift terms (see Vahidinia et al 2011 and section 7). The interface and interference terms are so significant in this case that they completely extinguish the "directly transmitted" beam before it gets through this layer. That is, its apparent optical depth τ, or more properly its extinction, is much larger than either higher or lower porosity layers containing the same mass in particles.

We can use DISORT to quantify the behavior of the layers as filling factor increases, starting with the classical case (section 5 and figure 11) where Mie theory leads to particle properties that adequately describe the diffuse scattering and extinction The reflected intensities are more well behaved, so we start there. Figure 13 shows the diffusely reflected intensities at 15.5μm wavelength, as functions of zenith angle, for filling factors of 0.09, 0.15, 0.02, and 0.50. In each case the smooth curves represent our best fit DISORT model, with τ chosen to give consistent intensities for the diffusely reflected and transmitted intensities. Deviation of τ from the classical independent scattering value is taken as evidence for deviation of Q_e from the classical value. The diffuse intensities also depend on ϖ_o, and so we can tell whether it is Q_s or Q_a that is changing, or both. We have made an attempt to adjust the phase function $P(\Theta)$ in plausible ways, to allow for the fact that monomer overlap leads to larger typical particle sizes as well as greater deviation from sphericity; to do this we applied the Pollack and Cuzzi (1979) semi-empirical adjustment to $P(\Theta)$, which has the effect of augmenting scattered energy at intermediate scattering angles. We have made no special attempt to truncate or remove the diffraction lobe, because for particles with these sizes, it is not straightforward to separate from other components refracted by or externally reflected from the particle.

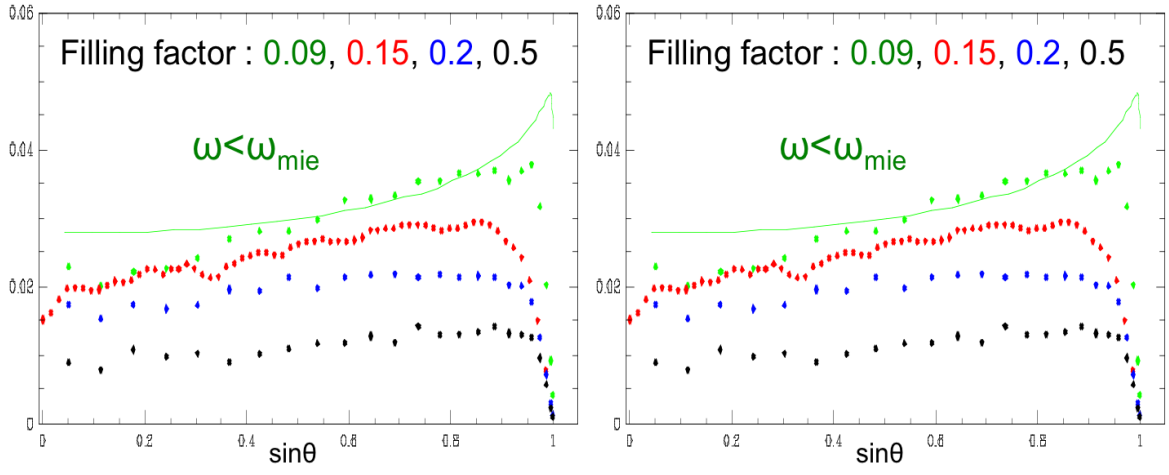

Fig. 13. It would be nice to model both the diffuse R and T, and the direct beam τ, for some or all four filling factors: 0.09, 0.15, 0.2, and 0.5.

porosity	ϖ_{Mie}	ϖ_{DDA}	τ_{Mie}	τ_{DDA}	c	d
0.0001	5.000e-10	0.0001	12	19.26	1.013e-08	1.234e+16
0.0001	1.000e-09	0.0001	10	8.578	3.339e-07	5.942e+14
0.0001	3.000e-09	0.0001	9	3.931	3.696e-05	6.764e+12
0.001	3.000e-09	0.0001	8	1.656	8.010e-05	3.932e+12
0.001	3.000e-09	0.0005	10	7.831	7.194e-06	1.233e+13
0.001	3.000e-09	0.001	11	19.73	6.971e-08	7.144e+14
0.01	1.000e-09	0.0001	12	5.421	1.951e-06	6.408e+13
0.01	1.000e-09	0.0005	11	5.404	1.723e-06	4.087e+13
0.01	1.000e-09	0.001	10	8.578	3.339e-07	1.879e+14

7. Toy model of the physics

8. Conclusions

We have developed a new end-to-end approach for modeling regolith radiative transfer for monomers of arbitrary size, shape, and packing density. The approach starts with adapting the Discrete Dipole model to a case with periodic horizontal boundary conditions, to mimic a small piece of a semi-infinite slab of regolith. The internal fields in the DDA target are then summed on a grid located in the near field, or more correctly the Fresnel zone, of the target layer. This 2D field is transformed to an angular emergent intensity field using the angular spectrum approach. The various parts of this approach have been thoroughly tested in several ways by comparison with theoretical behavior of a dielectric slab (Fresnel's analytical coefficients), including the angular behavior of specular reflection and transmission. The discrete monomer aspect of the code was tested by comparison with a classical multiple scattering technique (Mie scattering and the DISORT facility code).

Our primary result of interest from the standpoint of application to planetary regoliths, is that realistic porosity is out of the regime which can be properly treated by simple models; this has been known before, in fact (MC95). However, we do illustrate that a correct treatment of porosity *does* lead to better agreement with actual experimental data. That is, figure 1 shows that realistic layers have *higher* emissivity in transparency bands than predicted by any current model; our models show just the right behavior, in that layers with porosity in the realistic range have *lower* reflectivity than classical models that assume nominal grain properties, which by Kirchoff's laws, means higher emissivity. We show using a "toy model" that treats layered media, that increasing filling factor makes interface terms more important, lowering the reflectivity of individual "slabs" (monomers) below their independently scattering (Fresnel coefficient) values and lowering the reflectivity of the layered target below that which obtains when the "slabs" are widely spaced. This is consistent with our finding that the primary effect is a decrease in particle *albedo* ϖ_o.

The code is computationally demanding, and currently pushes the memory limits of NASA's largest massively parallel computers. However there is nothing but compute power to limit its scope of applications, and these limitations will become less restrictive in time. For instance, the first DDA case studied by Purcell and Pennypacker (1973) was limited to targets with very few dipoles.

Acknowledgements

We are very grateful to NASA's HEC program for providing the ample computing time and expert assistance without which this project would have been impossible. We'd like to thank Terry Nelson, and especially Art Lazanoff for help getting the optimizing done, Bob Hogan for parallelizing and automating other parts of the model, and Denis Richard for running a number of cases in a short time. The research was partially supported by the Cassini project, partially by a grant to JNC from NASA's Planetary Geology and Geophysics program, and partially by Ames' CIF program.

Appendix A: Porosity

Hapke (2008) presents a discussion of regimes of particle size-separation-wavelength space where particles may or may not be regarded as scattering independently and incoherently, an assumption on which current models of RRT are generally based. His results are summarized in his equation (23) and figure 2, in which a critical value of volume filling fraction ϕ is given at which coherent effects become important, as a function of D/λ where D is particle diameter. The model assumes the particles have some mean separation L. In cubic close-packing, 8 spheres each contribute 1/8 of their volume to a unit cell of side L. Thus the volume filling fraction $\phi = (4\pi D^3/24L^3) = \frac{\pi}{6}(D/(D+S))^3 = \pi/6(1+S/D)^3$ (Hapke 2008, equation 23). The physics is actually quite simple; it is assumed that coherent effects play a role when the minimum separation between particle *surfaces* $S = L - D < \lambda$, and the rest is algebra. The curve in figure 2 of Hapke 2008 is simply $\phi = \pi/(6(1+\lambda/D)^3)$, that is, merely substitutes $\lambda = S$ in the definition of filling factor. Nevertheless it graphically illustrates the expectation that traditional "independent scattering" models will be valid only at much smaller volume filling factors when $D/\lambda <$ several, than for $D/\lambda \gg 1$. Still it is based on a premise that coherency emerges when $S = L - D \leq \lambda$. In fact the asymptote at $D/\lambda \gg 1$ may only be due to the fact that in the sense of packing, the assumptions of the model equate this limit to $D/S \gg 1$, or the close-packing limit when changing volume density has little effect on anything. The premise is that of van de Hulst (1957), that coherency effects are negligible when the particle spacing exceeds several wavelengths (*cite page*).

In a model study of particle scattering at microwave wavelengths, Cuzzi and Pollack (1979; Appendix) hypothesized that coherent effects entered when the shadow length $l_s = D^2/2\lambda$

exceeded the distance to the next particle *along a particular direction*[2], $l^* = 4L^3/\pi D^2$. The distance l^* is different from the mean particle separation, or nearest neighbor distance, $l = N^{-1/3}$ where $N = 6\phi/\pi D^3$ is the particle number per unit volume.

It appears that, at least in the planetary science and astronomy literature, there are no more firm constraints than these. Our results are broadly consistent with these estimates, although we find nonclassical effects setting in at somewhat lower volume densities than these estimates would predict, in the regime where $D \sim \lambda$. *we haven't shown this yet..... Moreover, our results show that the effects of nonclassical behavior - even the sign of the deviation from classical predictions - depend on the refractive indices of the particles.* In future work, based on studies such as we present here, these simple limits can be improved and refined, and, perhaps, simple corrections may be developed which depend on particle refractive indices.

Appendix B: Need for near field sampling

Here we illustrate why the traditional application of the DDA code, in which the scattered fields have been evaluated at "infinity", introduces artifacts in our application, where the field scattered from a horizontally semi-infinite layer is being sought. For simplicity we consider a finite thickness dielectric slab with real refractive index n_r, illuminated at normal incidence by a plane wave with electric field $\mathbf{E_i}$. For a slab which is laterally infinite ($W \to \infty$) the wave inside and outside the slab can be easily solved for by equating boundary conditions at $z = 0$ and $z = H$ (see figure 14), resulting in explicit equations for the coefficients A and B, which then determine the internal fields, and the Fresnel reflection and transmission coefficients R and T (solutions found in many basic electrodynamics textbooks).

The first novelty in our application is implementation of periodic boundary conditions which mirror the TUC (of finite width W) laterally; this has the effect of removing edge effects in the internal fields and, for the dielectric slab, would ensure that the internal field, within the TUC of width W, obeys essentially the classical solution. However, the original procedure with this modeling, as in all previous applications of DDA, was to calculate the scattered field from the TUC (the "target") alone, and moreover at infinity, using the Fraunhofer approximation to the free space Green's function. Unfortunately this introduces artifacts into the solution we desire, which is that from a truly laterally infinite slab. Below we sketch the nature of these artifacts, and motivate our approach to avoid them.

We use the Fresnel approximation to the free-space Green's function (valid in general, not merely at infinity) to illustrate that the problem is not alleviated merely by making this simple change. In this case, the full solution for the scattered field at vector distance $\mathbf{r}$ is

[2]This is derived setting the expectation length l^* as that distance at which the probability of a "hit" on another particle is unity: $N(\pi D^2/4)l^* = 1$, giving $l^* = 4/\pi D^2 N = 4L^3/\pi D^2$.

given by

$$\mathbf{E}(\mathbf{r}) = \mathbf{E_i}(\mathbf{r}) + k^2(n_r^2 - 1) \int_V G(\mathbf{r}, \mathbf{r}')\mathbf{E_i}(\mathbf{r}')dV \tag{33}$$

where $k = 2\pi/\lambda$, the volume V represents the slab of thickness H and two-dimensional width W in (x, y), and

$$G(\mathbf{r}, \mathbf{r}') = \frac{e^{jk|\mathbf{r}-\mathbf{r}'|}}{4\pi|\mathbf{r} - \mathbf{r}'|} \tag{34}$$

is the free space Green's function, for which the Fresnel regime approximation is

$$G(\mathbf{r}, \mathbf{r}') \approx \frac{1}{4\pi z} e^{jk(z-z')} e^{\frac{j\pi}{2}[\frac{(x-x')^2}{F^2} + \frac{(y-y')^2}{F^2}]}, \tag{35}$$

where $F = \sqrt{\lambda z/2}$ is the Fresnel scale. The Fresnel approximation is valid when $(z - z')^2 \gg (x - x')^2, (y - y')^2$ but does assume $z \gg z'$; that is, it remains a far-field solution.

Substitution of equation (35) into equation (33) (for illustration we consider only $z > H$) then leads to:

$$\mathbf{E}(\mathbf{r}) = e^{jkz} + k^2(n_r^2 - 1)\frac{e^{jkz}}{4\pi z} \int_0^H e^{-jkz'}[Ae^{jk_1 z'} + Be^{-jk_1 z'}]dz' \int_{-W/2}^{W/2} e^{\frac{j\pi}{2}[\frac{(x-x')^2}{F^2} + \frac{(y-y')^2}{F^2}]}dx'dy'. \tag{36}$$

The above solution can be written as

$$\mathbf{E}(\mathbf{r}) = e^{jkz} + I_1(z)I_2(z), \tag{37}$$

where

$$I_1(z) = 2jF^2k^2(n_r^2 - 1)\frac{e^{jkz}}{4\pi z} \int_0^H e^{-jkz'}[Ae^{jk_1 z'} + Be^{-jk_1 z'}]dz' \tag{38}$$

$$I_2(z, W) = \int_{-W/2}^{W/2} e^{\frac{j\pi}{2}[\frac{(x-x')^2}{F^2} + \frac{(y-y')^2}{F^2}]}\frac{dx'}{F}\frac{dy'}{F}. \tag{39}$$

The function $I_2(z, W)$ is the Fresnel transform of a uniform square aperture of side W. Because our periodic boundary condition method ensures the internal field will assume its proper value for a laterally infinite target, we could make use of the plane-parallel solutions for the (known) coefficients A and B alluded to above in calculating $I_1(z)$ from equation (38). More directly, for purposes of illustration, we note that $I_1(z)$ is independent of W, so can be directly evaluated in the case $W \to \infty$, where the full solution is known at $z > H$ to be $\mathbf{E}(\mathbf{r}) = Te^{jkz}$ (see figure 14), and the integral $I_2(z)$ takes the form

$$I_2(z) = \frac{1}{2j} \int_{-\infty}^{\infty} e^{j\pi/2[\eta^2 + \zeta^2]}d\eta d\zeta = 1. \tag{40}$$

Then from equation (37), $I_1(z) = \mathbf{E}(\mathbf{r}) - e^{jkz} = (T - 1)e^{jkz}$. The *general result*, for finite W, then becomes

$$\mathbf{E}(\mathbf{r}) = e^{jkz} + (T - 1)e^{jkz}I_2(z, W). \tag{41}$$

To clarify the significance of the result, we add and subtract a term Te^{jkz} to equation (41), to get

$$\mathbf{E}(\mathbf{r}) = Te^{jkz} + (e^{jkz} - Te^{jkz}) + (T-1)e^{jkz}I_2(z,W) \tag{42}$$

$$= Te^{jkz} + (1-T)e^{jkz}[1 - I_2(z,W)] = \mathbf{E}_\infty(\mathbf{r}) + \mathbf{E}_\mathbf{W}(\mathbf{r}). \tag{43}$$

We can interpret this result as a superposition or modulation of the desired field $\mathbf{E}_\infty(\mathbf{r})$, arising from a slab which is laterally infinite, with a perturbation field $\mathbf{E}_\mathbf{W}(\mathbf{r})$ arising from the diffraction pattern of the truncated slab of finite width W. The perturbation term $\mathbf{E}_\mathbf{W}(\mathbf{r})$ (second term of final expression) vanishes either if the slab indeed does not interact with the incident wave ($T = 1$) or if the slab is infinitely wide ($W \to \infty$, in which case $I_2(z,W) \to 1$). It is essentially the Fresnel diffraction pattern of the area that is left out when an infinite slab is truncated to finite width W. In principle, the same approach can be used in the reflection regime $z < 0$, and a similar result is achieved. Indeed our initial numerical solutions which evaluated the scattered field from the TUC using the standard Fraunhofer free-space Green's function in the DDA code showed essentially this behavior, which we thus can identify as an artifact if our solutions are intended to apply to a laterally infinite slab of material.

To avoid the artifact we need to let our TUC extend to $W \to \infty$, in which case we *would* literally be in the "shadow" of the layer and edge effects would vanish. As this is numerically unfeasible, our solution instead is to nestle our sampling grid very close to our finite size TUC. That is, as noted above, the Fresnel solution above is valid when $(z-z')^2 \gg (x-x')^2, (y-y')^2$ *and* $z \gg z'$. More rigorously, it and the diffraction perturbation it contains (equation 42), apply outside the "shadow zone" of the slab, where $z > z_{shad} = W^2/2\lambda$ (see figure 3). Only for $z > z_{shad}$ have waves emanating from the perimeter of the slab had a chance to interact with each other and create the Fresnel diffraction pattern leading to the perturbation $I_2(z,W)$. Physically speaking, if our layer really *were* laterally infinite in extent, any sampling point *would* be within its "shadow" and the emergent intensity from the layer alone would be properly calculated without the perturbation due to a finite sized TUC.

At all times, however, we are wary not to place our sampling grid *too close* to the target surface, where evanescent effects might corrupt our signal; these fall off very quickly (roughly as z/λ^p), we have a procedure for detecting their presence (section 3) and we have not found them to be a problem as long as $z-H > \lambda$. The success of this strategy is shown in the various tests we have conducted (sections 4 and 5). Of course this logic applies mathematically for both $z > H$ and $z < 0$, but is easier to visualize for a "shadow" zone at $z > H$.

Appendix C: Fourier sampling

We use the formalism of the *angular spectrum*, described by Mandel and Wolf (1994, section 3.C). The angular spectrum $A(k_y, k_z)$ and the field on a grid $E(x_0; y, z)$ are often defined

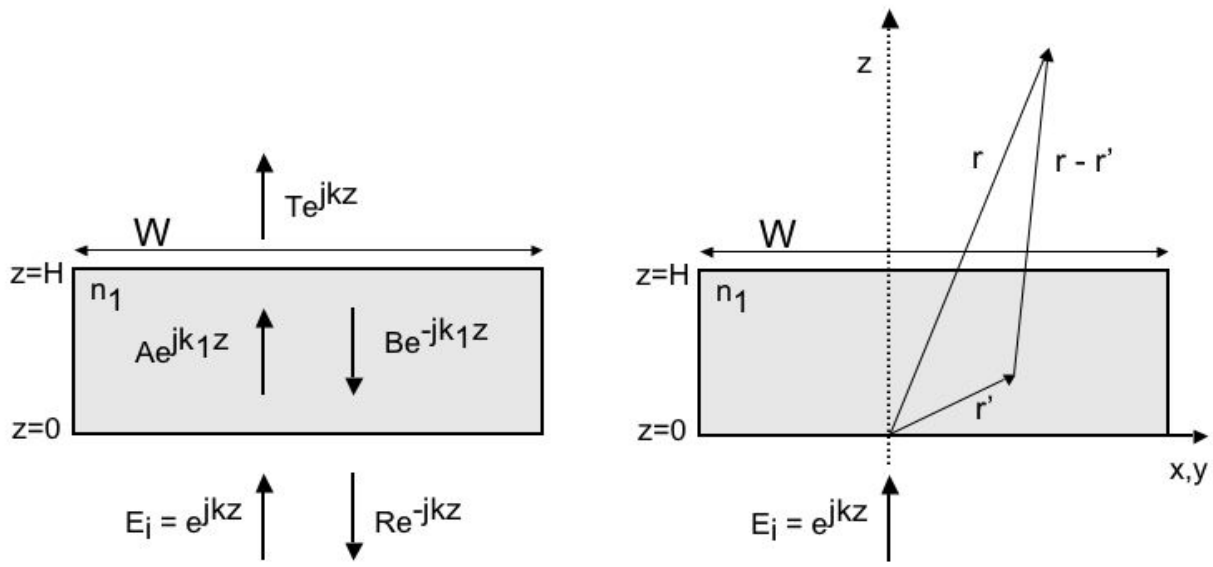

Fig. 14.

as infinite-domain Fourier transform pairs (see below). We will use the "cycles" definition of frequency (in our case, spatial frequency) rather than the "radians" definition used by Mandel and Wolf (MW) for simplicity; this removes floating factors of $(1/2\pi)$. We will retain the transform "direction" notation of MW, which is common (see also Blackman and Tukey method in Stoica and Moses 1997, SM97); in this convention the frequency-dependent function is obtained using the negative exponential. We note that Numerical Recipes (Press et al. 1999) adopts the opposite "direction" convention, which we feel leads to less intuitive results in the frequency domain. In the 1D case, with y spatial, and k spatial frequency, coordinates respectively, the infinite Fourier Transform reads:

$$g(k) = \int_{-\infty}^{\infty} f(y) e^{-2\pi i y k} dy \tag{44}$$

$$f(y) = \int_{-\infty}^{\infty} g(k) e^{2\pi i y k} dk \tag{45}$$

MW and other authors discuss the angular spectrum only in the context of the infinite Fourier Transform shown above, where the dimensions of $f(y)$ and $g(k)$ are different, but for practical reasons we will be using discrete or finite Fourier Transforms. This leads to subtle but important differences. In particular, changing to the *finite* transform pairs $f(y)$ and $a(k) = g(k)/L$ and then expressing them in their discrete series forms leads to:

$$a(k) = g(k)/L = \frac{1}{L} \int_{-L/2}^{L/2} f(y) e^{-2\pi i y k} dy \approx \frac{1}{N\Delta y} \sum_{l} f(y_l) e^{-2\pi i y_l k} \Delta y, \quad , \tag{46}$$

or, now also discretizing k:

$$a(k_\alpha) = \frac{1}{N} \sum_l f(y_l) e^{-2\pi i l\alpha/N} \tag{47}$$

$$f(y_l) = \sum_\alpha a(k_\alpha) e^{2\pi i l\alpha/N} \tag{48}$$

where $y_l = l\Delta y$, $k_\alpha = \alpha\Delta k$, and $\Delta k = 1/(N\Delta y)$ where N is the number of points in both the y and k arrays. Note that the dimensions of $f(y)$ and $a(k)$ are the same. This convention seems to be the more common one, in that the prefactor goes with the negative sign in the exponential, and the negative sign is used to generate the function defined in frequency space (SM97).

We thus trivially rewrite the transform pair of MW, using their equations 3.2-19,20,23,25, and 27, as

$$\mathcal{U}(k_y, k_z) = \int_{-\infty}^{\infty}\int_{-\infty}^{\infty} E(0, y, z) e^{-2\pi i(yk_y + zk_z)} dydz \tag{49}$$

$$E(0, y, z) = \int_{-\infty}^{\infty}\int_{-\infty}^{\infty} \mathcal{U}(k_y, k_z) e^{2\pi i(yk_y + zk_z)} dk_y dk_z. \tag{50}$$

The electric field E is sampled on the plane $x = x_0$ (note this is not the center of the layer); note that E and $\mathcal{U}$ have different dimensions.

We now consider the associated discrete Fourier transform, on the finite plane of dimension L^2. By analogy to the 1D case (equation 46) we define a slightly different vector transform function $A_i(k_y, k_z) = \mathcal{U}_i(k_y, k_z)/L^2$ (where $i = x, y, z$ component of each quantity) as the two-dimensional finite Fourier Transform of the 3D complex vector electric field strength $E_i(x_0; y, z)$ (x_0 can be chosen =0):

$$A_i(k_y, k_z) = \frac{1}{L^2} \int_{-L/2}^{L/2}\int_{-L/2}^{L/2} E_i(x_0; y, z) e^{-2\pi i(yk_y + zk_z)} dydz, \tag{51}$$

where we note as that in SM97, the numerical scaling prefactor is associated with the negative exponential transform into frequency space. This (finite) integral transform is readily replaced by a discrete summation, where we substitute $y_l = l\Delta$, $z_m = m\Delta$, $k_y = \alpha dk$, $k_z = \beta dk$, and l, m, α, and β are integers, where $\Delta = dy = dz$ is the grid spacing in the Cartesian (y, z) DDFIELD grid. From sampling theory, $dk = 1/L$ where L is the full linear extent of the 2D grid of $E(y, z)$ (the TUR, assumed to be square), and the maximum resolvable spatial frequency is $k_{max} = 1/\Delta$; typically $-k_{max/2} \leq (k_y, k_z) \leq k_{max}/2$. Then

$$A_i(k_y, k_z) = \frac{1}{(N\Delta)^2} \sum_{-N/2}^{N/2}\sum_{-N/2}^{N/2} E_i(x_0; y_l, z_m) e^{-2\pi i(l\alpha + m\beta)\Delta/N\Delta} \Delta^2 \tag{52}$$

$$A_i(k_y, k_z) = \frac{1}{N^2} \sum_{-N/2}^{N/2}\sum_{-N/2}^{N/2} E_i(x_0; y_l, z_m) e^{-2\pi i(l\alpha + m\beta)/N}, \tag{53}$$

where here $A_i(k_y, k_z)$ and $E_i(x_0; y_l, z_m)$ have the same units. Using this transform convention, the discrete form of Parseval's theorem reads

$$\sum_{\alpha}\sum_{\beta} |A_i(\alpha,\beta)|^2 = \frac{1}{N^2} \sum_{l}\sum_{m} |E_i(l,m)|^2, \tag{54}$$

which is intuitively meaningful because the wave's E field (nominal magnitude E_o) covers all N^2 points in the (y, z) grid, but the equivalent emerging plane wave only occupies a single grid cell in the (k_y, k_z) grid. The convention in Numerical Recipes makes less sense in our context. So, if $|E_o|^2$ is a spectral flux density (energy/area/time/wavelength interval) then so is $|A(\alpha,\beta)|^2$ (leaving aside issues of the permittivity of free space). This relationship was numerically verified in our code.

The orthogonal components E_x, E_y, and E_z are separately transformed and combined. The output A_x, A_y, A_z could be used to calculate polarization state (A_{par}, A_{perp}), which are both, by definition, perpendicular to the ray direction at (k_y, k_z), but because we are only interested in intensity, we simply sum the squares of A_i as noted above.

Overly coarse sampling of $k-$space can result in poor estimates of the locations and magnitudes of narrowly defined emergent rays; unfortunately the dimension of the DDFIELD grid is computationally constrained to some degree because our version of DDFIELD is extremely time consuming; a new, faster version is available at *http: Bruce's new DDFIELD Reference*. For now, we overcome this obstacle by zero-filling the array $E(x_0; y, z)$ out to some considerably larger extent L', retaining the original array as a subset. Upon transforming this larger array we achieve spatial frequency resolution $dk' = 1/L' \ll dk = 1/L$; this high resolution reveals the true locations and amplitudes of the peaks by over-resolving (at $dk' = 1/L'$) the intrinsic angular width in wave number space $dk = 1/L$. Tests conducted using this simple trick provided a very regular and reliable reconstruction in k-space of both the direction and amplitude of incident plane waves crossing the DDFIELD grid in a variety of directions. This is a valuable approach, because the compute time needed to converge a DDFIELD grid of size N^2 is roughly dependent on N^2, while the time needed to perform an FFT of a significantly zero-filled grid grows only as $N\log N$.

The more highly resolved plane wave fluxes $A_i'(k_y', k_z')$, are smaller in magnitude than a value which lies entirely in a single (k_y, k_z) bin and represents the entire plane wave. This is because, as *flux densities*, the more highly resolved results of the zero-filled calculation each represent the intensity integrated over a smaller solid angle. To obtain the total flux density in the wave, we would sum over the narrow "packet" of rays, each having angular width $dk_y' dk_z'$ lying in a scattered lobe of (larger) angular width $dk_y dk_z$. Nevertheless, an effective *intensity* can be determined for each of these rays, given by its flux divided by its corresponding solid angle. As defined this way, the intensity is invariant to zero-filling, because the flux in a (k_y, k_z) bin simply decreases with the angular width of the bin. That

is, $A_i'(k_y', k_z')/dk_y'dk_z' = A_i(k_y, k_z)/dk_y dk_z$. In section 3.C.1, we show how we determine true intensities (flux density per unit solid angle).

References

Blevin, W. R., and W. J. Brown (1961) Effect of particle separation on the reflectance of semi-infinite diffusers; J. Opt. Soc. Am. 51, 129-134

Conel, J. E. (1969) J. Geophysical Research, 74, 1614-1634

Cuzzi, J. N. (1985) Rings of Uranus - Not so thick, not so black; Icarus, 63, 312-316

Cuzzi, J. N. and Estrada, P. E. (1998) Icarus, 132, 1-35

Cuzzi, J. N., J. J. Lissauer, L. W. Esposito, J. B. Holberg, E. A. Marouf, G. L. Tyler, A. Boischot (1984). In Planetary Rings. Eds. R. Greenberg and A. Brahic. U. Arizona Press. Tucson, Arizona.

Draine, B. T. and Flatau, P. J. (1994) J. Opt. Soc. Am. 11, 1491-1499

Draine, B. T. and Flatau, P. J. (2008) Discrete-dipole approximation for periodic targets: theory and tests; J. Opt. Soc. Am. 25, 2693-2703

Edgar, A., G. V. M. Williams, and J. Hamelin (2006) Optical scattering in glass ceramics; Current Applied Physics 6, 355-358

Esposito, L.W., J.N. Cuzzi, J.B. Holberg, E.A. Marouf, G.L. Tyler, and C.C. Porco 1984. In Saturn. Eds. T. Gehrels and M Mathews. U. Arizona Press. Tucson, Arizona.

Göbel, G., J. Kuhn, and J. Fricke (1995) Dependent scattering effects in latex-sphere suspensions and scattering powders; Waves in Random Media, 5, 413-426

Goody, R. M. (1964) Limb darkening of thermal emission from Venus; Icarus, 3, 98-102

Hansen, J. E. (1969) Astrophys. J. 155, 565

Hansen, J. E. and Travis, L. D. (1974) Space Science Reviews 16, 527-610

Hapke, B. (1981) J. Geophys. Res., 86, 4571-4586

Hapke, B. (1983) BOOK

Hapke, B. (1999) J. Quant. Spectrosc. Rad. Transf. 61, 565-581

Hapke, B. (2008) Bidirectional reflectance spectroscopy, 6. Effects of porosity; Icarus, 195, 918-926

Irvine, W. M. (1975)

Ishimaru, A. and Y. Kuga (1982) Attenuation constant of a coherent field in a dense distribution of particles; J. Opt. Soc. Am. 72, 1317-1320

Linsky, J. 1972; A proof of the relation between reflectivity and emissivity in an isothermal scattering and absorptive atmosphere; J.Q.S.R.T. 12, 777-781

Lumme and Bowell 1981

Mandel, L. and Wolf, E., (1994) Optical Coherence and quantum optics (New York: Cambridge University Press)

Mishchenko, M. (1994) Asymmetry parameters of the phase function for densely packed scattering grains; J.Q.S.R.T. 52, 95-110

Mishchenko, M. and A. Macke (1997) Asymmetry parameters of the phase function for isolated and densely packed spherical particles with multiple internal inclusions in the geometric optics limit; J.Q.S.R.T. 57, 767-794

Moersch, J. E. and Christensen, P. R. (1995) Thermal emission from particulate surfaces: A comparison of scattering models with measured spectra; J. Geophysical Research, 100, 7465-7477

Mustard, J. F. and Hays, J. E. (1997) Effects of hyperfine particles on reflectance spectra from 0.3 to 25 μm; Icarus, 125, 145-163

Pitman, K. M., M. J. Wolff, and G. C. Clayton (2005) Application of modern radiative transfer tools to model laboratory quartz emissivity; J. Geophys. Res. 110, E08003

Plass, G.N., G.W. Kattawar, and F.E. Cathcings 1973. Appl. Opt., vol. 12, pp 314-329.

Pollack, J. B. and Cuzzi, J. N. (1979) J. Atmospheric Sciences, 37, 868-881

Poulet, F., D. Cruikshank, J. N. Cuzzi, and T. Roush (2003) Astronomy and Astrophysics 412, 305-316

Poulet, F., J. N. Cuzzi, D. Cruikshank, T. Roush, and C. Dalle Ore (2002a) Icarus, 160, 313-324

Press, W. H., S. A. Teukolsky, W. T. Vetterling, and B. P. Flannery, (1999) Numerical recipes in FORTRAN 77: the Art of Scientific computing (New York: Cambridge University Press)

Purcell, E. M., and C. Pennypacker (1973) Astrophys. J. 186, 705-714

Shepard, M. and P. Helfenstein (2007) A test of the Hapke photometric model; Journal of Geophysical Research, Volume 112, Issue E3, CiteID E03001

Shkuratov, Y. G., M. A. Kreslavsky, A. A. Ovcharenko, D. G. Stankevitch, and E. S. Zubko (1999a) Icarus 141, 132-155

Shkuratov, Y. G., Y. Starukhina, H. Hoffmann, and G. Arnold (1999b) Icarus 137, 235-246

Spilker, L. J., S. H. Pilorz, B. D. Wallis, S. M. Brooks, S. G. Edgington, F. M. Flasar, J. C. Pearl, M. R. Showalter, C. Ferrari, R. K. Achterberg, C. A. Nixon, P. A. Romani, and the Cassini CIRS Team (2005) 36th LPSC, League City, Texas, abstract no. 1912

Spitzer and Kleinman

Stoica, P. and Moses R. L., (1997) Introduction to Spectral Analysis (New Jersey: Prentice Hall)

van de Hulst, H. C. (1980) Multiple Light Scattering; Academic Press

van de Hulst, H. C. (1981) Light scattering by small particles, Dover

Van oosterom, A., and Strackee J. (1983) IEEE, BME-30 125-126

Wald, A. E. (1994) Modeling thermal infrared (2-14μm) reflectance spectra of frost and snow; J. Geophys. Res. 99, B12, 24241-24250

Wald and Salisbury 1995

Wenrich, M. L. and P. R. Christensen (1996) Optical constants of minerals derived from emission spectroscopy: application to quartz; J. Geophys. Res. 101, B7, 15921-15931

Wiscombe, W.J., 1975a. J. Quant. Spectrosc. Radiative Transfer, vol 16, pp. 477-489.

Wiscombe, W.J., 1975b. J. Quant. Spectrosc. Radiative Transfer, vol 16, pp. 637-658.